Macalester Journal of Physics and Astronomy

Volume 10
Issue 1 *Spring 2022*

Article 5

May 2022

Molecular Line Search in Archival ALMA Imaging of M87

Xueyi Li
Macalester College, xli@macalester.edu

Molecular Line Search in Archival ALMA Imaging of M87

Abstract

We present a molecular line search in spectral imaging of the elliptical galaxy M87 using archival data from the Atacama Large Millimeter/sub-millimeter Array (ALMA). The primary goal of this project is to verify and characterize possible CO transition lines, which can be used for future studies to determine the dynamics of the system, or the mass of the supermassive black hole (BH) in the center of the galaxy. After performing extensive atmospheric modeling, we found that most of the absorption features have a corresponding atmospheric ozone transition, so it is unlikely that these features are either Galactic or extragalactic. We also found and corrected a calibration error that introduced an overly sharp absorption feature. After careful continuum subtraction, we calculated line strengths of these absorption features and identified CO emission from high-velocity gas very near the central BH. After analyzing the CO absorption and emission properties, we present a pathway forward for future spectral imaging programs of M87.

MACALESTER COLLEGE

Molecular Line Search in Archival ALMA Imaging of M87

by

Alex Li

in the

Department of Physics and Astronomy

Advisors: Benjamin Boizelle, Anna Williams

April 2022

MACALESTER COLLEGE

Abstract

Department of Physics and Astronomy

by Alex Li

We present a molecular line search in spectral imaging of the elliptical galaxy M87 using archival data from the Atacama Large Millimeter/sub-millimeter Array (ALMA). The primary goal of this project is to verify and characterize possible CO transition lines, which can be used for future studies to determine the dynamics of the system, or the mass of the supermassive black hole (BH) in the center of the galaxy. After performing extensive atmospheric modeling, we found that most of the absorption features have a corresponding atmospheric ozone transition, so it is unlikely that these features are either Galactic or extragalactic. We also found and corrected a calibration error that introduced an overly sharp absorption feature. After careful continuum subtraction, we calculated line strengths of these absorption features and identified CO emission from high-velocity gas very near the central BH. After analyzing the CO absorption and emission properties, we present a pathway forward for future spectral imaging programs of M87.

Acknowledgements

I would like to give special thanks to the following people, without whom I would not be able to complete this research project and this honors thesis:
Benjamin Boizelle, my research supervisor at Brigham Young University. I want to thank him for offering this research opportunity and his assistance in every step in completing the research project.
Anna Williams, my advisor at Macalester College since the second semester of my freshman year. I want to thank her for all of her support every since she became my advisor at Macalester.
Everyone else in the Physics and Astronomy department of Macalester College and my friends, who offered either direct or indirect help throughout my completing of this thesis.
Brigham Young University Physics and Astronomy department for the student funding for this student summer research project.

Contents

List of Figures

List of Tables

CHAPTER 1: Introduction

A galaxy is a gravitational bound system, composed mainly of stars, interstellar gas, dust, and dark matter. Depending on the geometric structure, galaxies are divided into four categories: spiral galaxies, elliptical galaxies, irregular galaxies, or lenticular galaxies. Spiral galaxies contain spiral arms extending from the central bright bulge. Elliptical galaxies have an elliptical shape and smooth distribution of light. Lenticular galaxies are in-between elliptical galaxies and spiral galaxies, with a less active disk in terms of star formation comparing to spiral galaxies. Irregular galaxies are galaxies that do not have a distinct regular shape and do not fall into any previous three categories.

At the center of nearly every large galaxy lies a supermassive black hole (SMBH), whose mass typically ranges between $10^6 - 10^9\ M_\odot$. Accretion disks around the black holes (BH) are formed when matter accretes onto the BHs. Gas in the disk falling into the BH heats up due to friction, during which process energy is released in the form of electromagnetic radiation. This produces a bright active nucleus that can – in rare cases – outshine the stellar light from its host galaxy. Despite their large masses, these BHs only dominate the gravity of the center-most regions of each galaxy, and detecting their kinematic influence typically requires high angular resolution observations and very sensitive instruments.

M87 is an elliptical galaxy with an actively accreting SMBH at its center. This accretion powers thermal emission from a small disk (∼50 parsecs in radius), with some of these emissions ejected in jets that extend nearly to the edge of the galaxy ($>$ 25 kpc) (Event Horizon Telescope Collaboration et al. 2019). Hubble Space Telescope (HST) Space Telescope Imaging Spectrograph (STIS) observations of ionized atomic gas tracers have revealed rotation-dominated gas kinematics in the accretion disk of M87. Recent EHT images have shown an emission ring of $\sim 39\mu$s and a shadow region of $\sim 10\mu$s, but there hasn't been any published work showing how these structures are connected (Event Horizon Telescope Collaboration et al. 2019). Thin-disk modeling produces a BH mass of $(3.5^{+0.9}_{-0.7}) \times 10^9\ M_\odot$ (Walsh et al. 2013), although these gas-dynamical models suffer from potentially serious

systematic uncertainties due to turbulence in the hot ($T \sim 10^4$ K) gas. Stellar-dynamical modeling (Gebhardt & Thomas 2009; Schulze & Gebhardt 2011) and later General Relativistic simulations of Event Horizon Telescope observations (Event Horizon Telescope Collaboration et al. 2019) found a higher BH mass of about 6.5×10^9 $M_\odot$ with about 10% precision, in clear tension with the gas-dynamical measurement, although additional modeling systematics have yet to be explored.

An alternative – and often more precise (e.g., Boizelle et al. 2019; North et al. 2019) – avenue to determine the BH mass uses dynamical cold kinematic tracers, which are gases with high abundance in the clouds within galaxies and are visible on the spectra. Properties of the transition lines of these gases thus as line shifts in wavelength and line strengths can be used to study the kinematics of the clouds. Although H_2 is the most abundant gas in the gas clouds around the galaxies, it has no dipole moment and is hard to detect its features in the spectrum. Thus emission from other molecules – like the next most commonly occurring molecule in a typical accretion disk of a galaxy, carbon monoxide (CO) – are used instead to trace cold gas clouds. Roughly half of all elliptical and lenticular galaxies have a detectable amount of gas and/or dust; for about 10% of all early type galaxies (ETGs), this gas and dust is concentrated in a circumnuclear disk with a radius of between ∼50–5,000 pc (Boizelle et al. 2017). No dust features are detected in optical HST imaging (Walsh et al. 2013), and previous surveys have not detected CO in the center of M87, either in emission or absorption, as shown in Figure 1.1 (e.g., Bieging et al. 1981; Braine & Wiklind 1993). Based on these earlier mm/sub-mm observations, CO(1−0) upper limits of ∼4 Jy km s^{-1} translates to constraints on the central H_2 mass of $< 10^7$ $M_\odot$.

Many of these ETGs exhibit emission lines from hot (∼10^4 K), partially ionized gas that primarily arises from the active galactic nucleus. Although there is not a clear connection between the atomic and molecular-phase gas distributions at the centers of these galaxies, absorption-line features against a bright nucleus can allow for estimates of the column density (N_H) of atomic gas along that line of sight. Both Dwarakanath et al. (1994) and Sabra et al. (2003) find evidence for moderate column densities of atomic gas, with $N_H \sim 10^{19-20}$ H particles per cm^2.

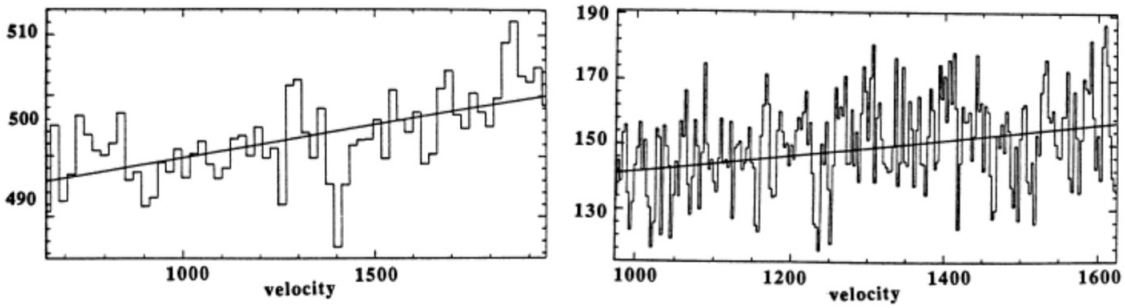

FIGURE 1.1: Spectra covering the CO(1-0) (left) and CO(2-1) (right) transitions of M87, in mK units. No clear emission or absorption is seen about the galaxy's systemic velocity of ∼1280 km s^{-1} beyond the observed noise level. Figure adapted from Braine & Wiklind (1993).

Because of its unparalleled sensitivity and angular resolution at millimeter/sub-millimeter wavelengths, Atacama Large Millimeter/Sub-millimeter Array (ALMA) is uniquely capable of detecting faint signatures of molecular gas, especially in extragalactic targets. Careful observations with ALMA have demonstrated sensitivity to CO emission in nearby galaxies down to the level of $10^5 - 10^6$ $M_\odot$. Less commonly, a CO transition is seen in absorption against the bright continuum of an actively accreting BH (Boizelle et al. 2017).

As a bright source of continuum emission from radio to mm wavelengths, M87 is an ideal target for ALMA imaging. While ALMA has accumulated a rich set of M87 observations that cover a variety of molecular line frequencies, there are still no published molecular gas measurements that cover the nucleus. With 11 archival observations covering CO transition bands, we hoped to take advantage of the capability of ALMA and provide some analyses regarding CO gas properties for future studies. Information about all the observations, including the time of observation, frequency bandwidths, antennae baselines, etc., are included in Table 2.1 of Chapter 2. In 5 of these observations, we find evidence for molecular absorption feature in the CO(1−0), CO(2−1), and CO(3−2) transitions. In 2 of these observations, we detect diffuse, high-velocity emission features around the CO(1−0) absorption line; in another, we see what appears to be CO(3−2) emission.

We investigated whether the absorption features are extragalactic in origin in two approaches. One way is to compare the ratios of observed frequencies and frequencies in the galaxy's rest frame. The other method models atmospheric effects

using `am`, a tool that calculates transmission of electromagnetic waves through Earth's atmosphere layers. Based on the model, the program performs quantitative analysis for radiative transfer from microwave to sub-millimeter frequencies. While atmospheric transmission modeling is crucial for investigating faint spectral line features in the radio band, such techniques like `am` are rarely employed. By exploring the functionality and applications of `am` in millimeter/sub-millimeter astronomy, we aimed to confirm or rule out atmospheric origins for observed absorption. We present our `am` results in Section 2.5.

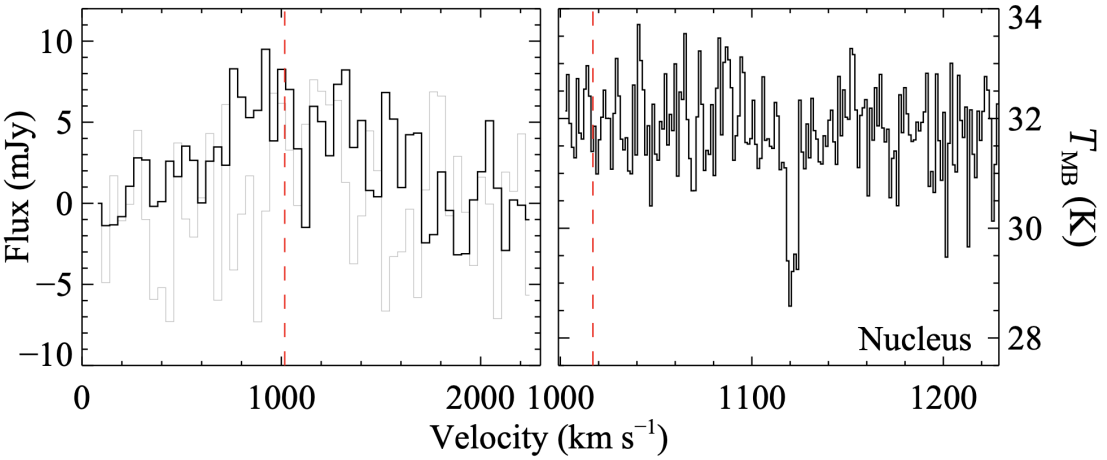

FIGURE 1.2: ALMA continuum imaging about the CO(2−1) transition of another active galaxy, NGC 4374. In addition to a diffuse but noticeable rise in flux densities near the systemic velocity (red dotted line) arising from CO(2−1) emission, the spectrum centered on the nucleus shows a distinct absorption feature that suggests moderately dense gas with a column density $N_{H_2} \sim 5 \times 10^{21}$ cm^{-2}. Figure adapted from Boizelle et al. (2017).

Numerical analyses on these features were performed both before and after the atmospheric modeling. Due to their intrinsic Gaussian-like shape, each of the potential absorption and emission features were fit with a Gaussian model. The three Gaussian parameters and the parameters of the linear function fitting the continuum were then obtained by numerical calculations with Python functions. In one case, the abnormally strong absorption line was decomposed into multiple component. We describe our fitting methods in Section 3.2 and results in Section 4.2.

With the absorption and emission data in hand, we examined the strength of absorption (W_{CO}) and emission-line (I_{CO}) strengths to explore the conditions and

dynamics at the center of M87. Analysis of $W_{\rm CO}$ and $I_{\rm CO}$ reveal intrinsic properties of the galaxy, such as the column density of molecular hydrogen gas along line of sight, the distance of the gas from the AGN center, and the velocity distribution, assuming CO gas is in circular motion around the AGN. The calculation of $W_{\rm CO}$ and $I_{\rm CO}$ and corresponding analysis are demonstrated in Chapter 4.

In Chapter 5, we conclude and discuss future prospects for CO absorption and emission-line studies using ALMA. Throughout this work, we assume a distance of 17.9×10^6 pc to M87 (Walsh et al. 2013), which corresponds to an angular scale of $\sim$90 pc arcsec^{-1}.

CHAPTER 2: Data

2.1 Observations

Table 2.1: M87 ALMA Imaging

Obs. date (1)	ν_{sky} **(GHz)** (2)	$\triangle\nu_{sky}$ **(MHz)** (3)	**Baseline (km)** (4)	$\theta_{major} \times \theta_{minor}$ θ_{PA} (5)	**MRS (arcsec)** (6)	**Time (hrs)** (7)	**rms (mJy beam^{-1})** (8)	**PWV (mm)** (9)	**Pol.** (10)
2012.1.00661.S (PI: Vlahakis)									
7 Mar 2014	99.90–101.89 101.78–103.76 111.92–113.91 113.85–115.72	31.25 31.25 31.25 0.977	0.015–0.423	2.″03 × 1.″42 60.2°	12.5	1.71	1.46	1.41	XX YY
28 Jan 2014	331.50-333.48 333.30-335.29 343.41–345.28 345.30–347.29	31.25 31.25 31.25 0.977	0.015–0.423	1.″16 × 0.″60 -83.7°	6.04	1.89	0.058	0.97	XX YY
2013.1.00073.S (PI: Tan)									
14 Jun 2015	213.00-214.99 215.00-216.99 228.63–230.50 230.57–232.56	31.25 31.25 0.977 31.25	0.021–0.784	0.″54 × 0.″44 -47.8°	4.04	0.25	1.23	0.69	XX YY
	213.00-214.99	31.25							

Continued on next page

Table 2.1: M87 ALMA Imaging

Obs. date (1)	ν_{sky} **(GHz)** (2)	$\triangle\nu_{sky}$ **(MHz)** (3)	**Baseline (km)** (4)	$\theta_{major} \times \theta_{minor}$ θ_{PA} (5)	**MRS (arcsec)** (6)	**Time (hrs)** (7)	**rms (mJy beam^{-1})** (8)	**PWV (mm)** (9)	**Pol.** (10)
16 Aug 2015	215.00-216.99 228.63–230.50 230.57–232.56	31.25 0.977 31.25	0.043–1.574	0.″27 × 0.″22 14.3°	1.88	0.50	1.98	0.74	XX YY
2013.1.01022.S (PI: Asada)									
8 Mar 2015	89.51–91.48 91.45–93.42 228.63–230.50 230.57–232.56	62.50 62.50 62.50 62.50	0.041–2.070	0.″46 × 0.″38 30.0°	23.8	3.32	0.236	1.56	XX YY YX YY
2015.1.00030.S (PI: Vlahakis)									
3 Nov 2015	99.88–101.86 101.87–103.86 112.28–114.16 113.85–115.72	31.25 31.25 1.13 1.13	0.085–16.20	0.″10 × 0.″046 -56.5°	0.97	0.66	0.306	0.96	XX YY
2015.1.01170.S (PI: Asada)									
3 Nov 2015	89.50–91.47 91.44–93.41 101.50–103.47	62.50 62.50 62.50	0.085–16.20	0.″10 × 0.″046 -56.5°	0.97	0.66	0.306	0.96	XX YY

Continued on next page

TABLE 2.1: M87 ALMA Imaging

Obs. date (1)	ν_{sky} **(GHz)** (2)	$\triangle\nu_{sky}$ **(MHz)** (3)	**Baseline (km)** (4)	$\theta_{major} \times \theta_{minor}$ θ_{PA} (5)	**MRS (arcsec)** (6)	**Time (hrs)** (7)	**rms (mJy beam^{-1})** (8)	**PWV (mm)** (9)	**Pol.** (10)
	113.85–115.72	62.50							
2012.1.00661.S (PI: Vlahakis)									
7 Mar 2014	99.90–101.89	31.25	0.015–0.423	2.″03 × 1.″42 60.2°	12.5	1.71	1.46	1.41	XX YY
	101.78–103.76	31.25							
	111.92–113.91	31.25							
	113.85–115.72	0.977							
28 Jan 2014	331.50-333.48	31.25	0.015–0.423	1.″16 × 0.″60 -83.7°	6.04	1.89	0.058	0.97	XX YY
	333.30-335.29	31.25							
	343.41–345.28	31.25							
	345.30–347.29	0.977							
2013.1.00073.S (PI: Tan)									
14 Jun 2015	213.00-214.99	31.25	0.021–0.784	0.″54 × 0.″44 -47.8°	4.04	0.25	1.23	0.69	XX YY
	215.00-216.99	31.25							
	228.63–230.50	0.977							
	230.57–232.56	31.25							

Continued on next page

TABLE 2.1: M87 ALMA Imaging

Obs. date (1)	ν_{sky} **(GHz)** (2)	$\triangle\nu_{sky}$ **(MHz)** (3)	**Baseline (km)** (4)	$\theta_{major} \times \theta_{minor}$ θ_{PA} (5)	**MRS (arcsec)** (6)	**Time (hrs)** (7)	**rms (mJy beam^{-1})** (8)	**PWV (mm)** (9)	**Pol.** (10)
	213.00-214.99	31.25							

Continued on next page

TABLE 2.1: M87 ALMA Imaging

Obs. date (1)	ν_{sky} **(GHz)** (2)	$\triangle\nu_{sky}$ **(MHz)** (3)	**Baseline (km)** (4)	$\theta_{major} \times \theta_{minor}$ θ_{PA} (5)	**MRS (arcsec)** (6)	**Time (hrs)** (7)	**rms (mJy beam^{-1})** (8)	**PWV (mm)** (9)	**Pol.** (10)
16 Aug 2015	215.00-216.99 228.63–230.50 230.57–232.56	31.25 0.977 31.25	0.043–1.574	0.″27 × 0.″22 14.3°	1.88	0.50	1.98	0.74	XX YY
2013.1.01022.S (PI: Asada)									
8 Mar 2015	89.51–91.48 91.45–93.42 228.63–230.50 230.57–232.56	62.50 62.50 62.50 62.50	0.041–2.070	0.″46 × 0.″38 30.0°	23.8	3.32	0.236	1.56	XX YY YX YY
2015.1.00030.S (PI: Vlahakis)									
3 Nov 2015	99.88–101.86 101.87–103.86 112.28–114.16 113.85–115.72	31.25 31.25 1.13 1.13	0.085–16.20	0.″10 × 0.″046 -56.5°	0.97	0.66	0.306	0.96	XX YY
2015.1.01170.S (PI: Asada)									
3 Nov 2015	89.50–91.47 91.44–93.41 101.50–103.47	62.50 62.50 62.50	0.085–16.20	0.″10 × 0.″046 -16.5°	0.97	0.66	0.306	0.96	XX YY

Continued on next page

TABLE 2.1: M87 ALMA Imaging

Obs. date (1)	ν_{sky} **(GHz)** (2)	$\triangle\nu_{sky}$ **(MHz)** (3)	**Baseline (km)** (4)	$\theta_{major} \times \theta_{minor}$ θ_{PA} (5)	**MRS (arcsec)** (6)	**Time (hrs)** (7)	**rms (mJy beam^{-1})** (8)	**PWV (mm)** (9)	**Pol.** (10)
	113.85–115.72	62.50							

Researchers have accumulated a number of observations of the nucleus of M87, which is a bright source (∼0.75–2.1 Jy) in various ALMA radio bands (Band 3, 84–116 GHz, Band 6, 211—275 GHz, and Band 7, 275 – 373 GHz). Despite the broad publicity of the Event Horizon Telescope and the role of ALMA in resolving the BH shadow of M87, these and other ALMA observations of the nucleus have never been used for CO transition studies, even when specifically sought for that purpose. My research mentor Dr. Boizelle obtained a total of 11 data sets in the public domain from the ALMA Science Archive[1]. These ALMA observations were made over a span of about 4 years by different Principle Investigators.

M87 has a redshift of $z \approx 0.00428$[2], which corresponds to a line-of-sight velocity $cz \approx 1284$ km s^{-1}. Assuming that the CO(1−0), CO(2−1), and CO(3−2) transitions have the same average redshift values as M87, the observed frequencies of these transition lines are 114.78 GHz, 229.56 GHz, and 344.32 GHz, respectively, according to Splatalogue[3]. We selected the observations that cover these three frequencies in hope of finding CO transitions with the high spectral resolution of ALMA.

We provide a quick overview of these 11 observations in Table 1, ALMA Imaging. The first three columns of Table 1 (ALMA Imaging) include the observation dates, frequency ranges, and frequency steps, or binning, of each observation. These observations cover a range of ∼90 GHz up to ∼350 GHz which includes CO(1−0) (114.78 GHz), CO(2−1) (229.56 GHz), and CO(3−2) (344.32 Ghz) transitions. Some programs have multiple observations on different dates and cover different ALMA Bands. For instance, in 2012.1.00661.S, one observation on Mar 7 2014 covers the CO(1−0) transition at 114.78 GHz; the other on Jan 28 2014 covers the CO(3−2) transition at 344.43 GHz. All 11 observations have four segments in frequency space or four spectral windows. Table 1 also includes the baseline step-up of ALMA configuration (Column 4), synthesized beam size of final imaging (Column 5), Maximum recoverable scale in arcsec (Column 6), total time of observation in hours (Column 7), background root-mean-square (rms) level in

[1] https://almascience.nrao.edu/aq/?result_view=observation

[2] https://ned.ipac.caltech.edu/byname?objname=M87&hconst=67.8&omegam=0.308&omegav=0.692&wmap=4&corr_z=1

[3] https://splatalogue.online//index.php

mJy beam^{-1} (Column 8), precipitate water vapor (PWV) in mm (Column 9), and polarization setup (Column 10).

Among the 11 programs, 3 observations cover the CO(1−0) transition at 114.78 GHz. Program 2012.1.00661.S (Mar 7) covers 113.85–115.72 GHz and has a smaller channel binning, or $\Delta\nu_{sky}$, of 0.977 GHz. The other three spectral windows covering different frequency ranges have larger $\Delta\nu_{sky}$ of 31.25 GHz and lower spectral resolution. Program 2015.1.00030.S has a continuous frequency range from 99.88 GHz to 115.72 GHz with slightly more coarse spectral resolution of 1.13 GHz in 112.28–115.72 GHz. The two spectral windows in 2015.1.00030.S, one covering 112.28–114.16 GHz and the other covering 113.85–115.72 GHz, overlap with each other in 113.85–114.16 GHz. Combining these two spectral windows provides a continuous spectrum of 112.28–115.72 GHz and covers the diffuse emission features that span a larger frequency range than is covered by a single spectral window. The diffuse emission possibly originated from a CO cloud with a velocity gradient. This will produce an emission feature that spans a broader frequency range. Program 2016.1.00021.S is similar to program 2015.1.00030, with some overlap between its spectral windows. Combining its spectral windows also gives a longer continuous spectrum from 112.00 GHz to 115.91 GHz and covers broad diffuse emission features.

The three observations that the cover CO(2−1) transition at an observed frequency of 229.56 GHz are programs 2013.1.00073.S, 2016.1.01154.V, and 2017.1.00841.V. Program 2013.1.00073.S has two observations with identical frequency coverage and channel binning, but the baseline configurations and synthesized beam sizes from these two observations are different from each other by a factor of two. However, in both observations, the spectral window that covers 228.63–230.50 GHz has a more narrow channel binning of 0.977 GHz than the other three spectral windows that are placed to measure continuum properties. Program 2016.1.01154.V is an EHT project with three observations. They have identical spectral coverage of 212.17–230.04 GHz with some gaps between spectral windows and identical spectral resolution of 7.81 GHz. With program 2017.1.00841.V, we imaged observations on Apr 20, 2018 and Apr 21, 2018. Program 2017.1.00841.V and 2016.1.01154.V have the same spectral coverage and spectral resolutions.

The only observation that covers the CO(3−2) transition at 344.32 GHz is program 2012.1.00661.S (Jan 28 2014). It has a spectral coverage of 331.50–335.29 GHz and 343.41–345.30 GHz. The third spectral window covering 343.41–345.28 GHz has a higher spectral resolution of 0.977 GHz compared to the of other spectral windows. See Table 1 for details of each observation.

2.2 Calibration and Imaging

After retrieving the raw visibilities from the ALMA Science Archive, Dr. Boizelle performed standard pipeline calibration using the Common Astronomy Software Applications (CASA) and the scriptForPI.py script provided by ALMA. This included bandpass, phase, and flux calibration using primarily quasar calibrators. In each case, the same pipeline versions of CASA that performed the scriptForPI.py were used. I ran self-calibration procedures following the CASA guide "First Look at Self Calibration"[4] for one MS of program 2013.1.00073.S. For the sake of time, Dr. Boizelle ran self-calibration and imaging on the remaining observation with CASA version 5.4.

For each loop of the self-calibration process, `tclean` task was executed to first interactively clean the residuals in the background and create a model. With the interactive interface of `tclean`, a circle was drawn to mark the central bright pixels as the source itself. We cleaned the image with this model until the noise in the background of the residual is comparable to the noise near M87. The model was saved when exiting `tclean` task. Then `gaincal` and `applycal` tasks were used to measure and apply phase and amplitude corrections. Another image was made with `tclean` and cleaned until we saw that the background noise was comparable to the noise near M87. We finished cleaning and exported .FITS images of M87.

These imaged .FITS data cubes consist of a spatial intensity map at many channels for each spectral window. All the observations were imaged with their native channel binning and over the frequency ranges for each spectral window listed in Table 1. Figure 2.1 shows an example of one of the channel maps of M87 at 229.36 GHz from program 2013.1.00073 (16 Aug 2015). This image extends beyond the

[4] https://casaguides.nrao.edu/index.php?title=First_Look_at_Self_Calibration

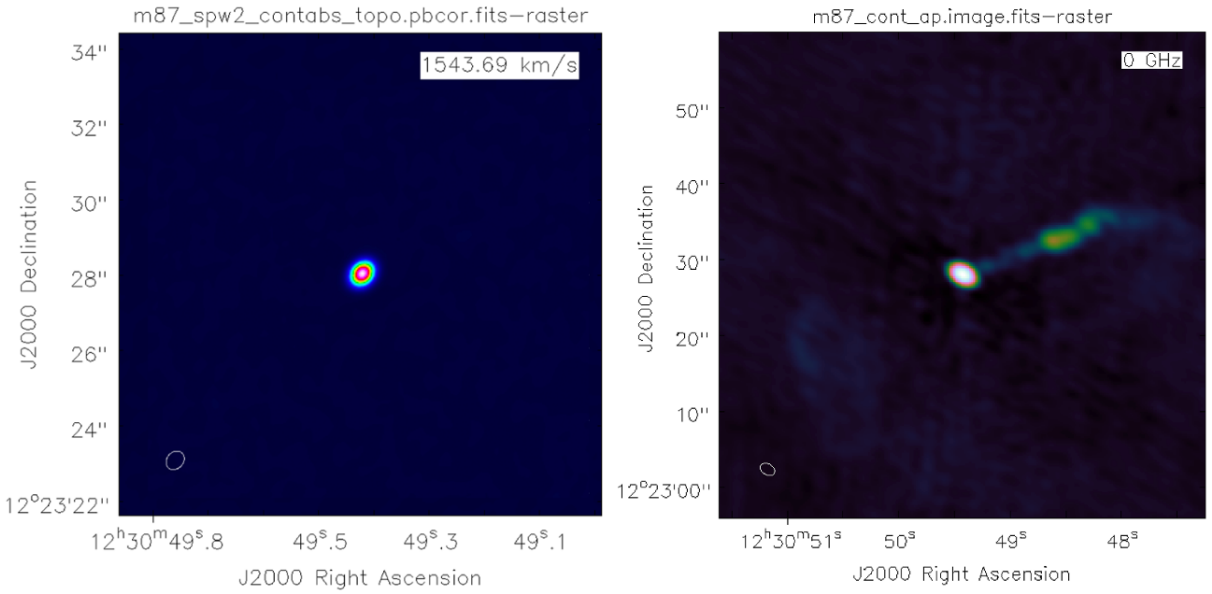

FIGURE 2.1: M87 channel map at v=1507.5 km/s (or at 229.36 GHz) from program 2013.1.00073.S with beam size of about 0.25″ and an rms noise of about 2.0 mJy beam^{-1} (left). The active nucleus is essentially completely unresolved. Although our sample includes observations across 4 years, this is representative of mm/sub-mm continuum images of M87. In some of these low-ν observations, the jet extending from the radio band to the optical is visible in the ALMA continuum images. Jet emission from M87 is on a scale of ∼20.3″, equivalent to 18 pc, measured from the brightest pixel in the center to roughly the end of the green region to the right.

size of the primary beam and shows that the continuum emission from M87 is very bright at the center. The background rms noise is 1.98 mJy beam^{-1} and the brightest pixel in the center has a flux density of 1.698 Jy. We imaged 3840 channels from 228.63 GHz to 230.50 GHz for program 2013.1.00073.S (16 Aug 2015). We extracted the continuum by integrating the flux densities over the full beam shape and by extracting the flux densities of the central pixel of the image, which is the brightest pixel of our source. These spectra are presented in Section 2.3

2.3 Spectra

We present all the continuum spectra (Figures 2.2-2.7) that contain a potential CO transition line in this section. The black continuum spectra are the flux densities

integrated over approximately the entire full synthesized beam shape and the red continuum spectra are the flux densities extracted on the central brightest pixel of our image. The dotted vertical lines mark CO transitions at $z = 0.00428$ and are labeled with the specific transition.

Both programs 2012.1.00661.S (Figure 2.2) and 2016.1.00021.S (Figure 2.4) show some absorption features at frequencies slightly above 114.78 GHz. Assuming these are real CO(1−0) absorption features, the slight discrepancy of ~ 8 MHz between the observed redshifted and rest-frame frequencies of this CO absorption line could be due to the slight changes in the line-of-sight motion of gas within M87. Two roughly symmetrical, broad bumps on either side of the 114.78 GHz are present in both programs 2015.1.00030.S (Figure 2.3) and 2016.1.00021.S (Figure 2.4). These features could be diffuse CO(1−0) emission from either side of a gaseous disk in circular rotation or emission from outflowing gas with a distribution of radial velocities. Such emission features can potentially reveal the dynamical structure of the CO gas within the galaxy. Detailed analysis of these lines is provided in Chapter 4.

The observations that cover CO(2−1) transition at 230 GHz are programs 2013.1.00073.S (Figure 2.5), 2016.1.01154.V (Figure 2.6), and 2017.1.00841.V (Figure 2.7). While we only see systematic noise present in other continuum spectra at frequencies where we expect a CO transition line, program 2013.1.00073.S (16 Aug, 2015) is the only MS with an absorption line at 229.60 GHz, with a line depth of 20 times greater than the noise in the continuum. The frequency of the absorption line also deviates from the predicted frequency at 229.59 GHz. However, the other MS from program 2013.1.00073.S (14 Jun 2015), observed three months prior, does not show any obvious transition at the same frequency. This strong, time-dependent feature caused us to more closely examine the data reduction script. We will discuss this in greater detail in Section 2.4. Programs 2016.1.01154.V (Figure 2.6) and 2017.1.00841.V (Figure 2.7) are Event Horizon Telescope (EHT) programs with global collaboration. Some fluctuations that occur repetitively at roughly constant frequency intervals are present in the spectra for these programs. While they are consistent and presented in these .V programs, we do not observe this type of fluctuation in other .S programs. This might be related to the .V

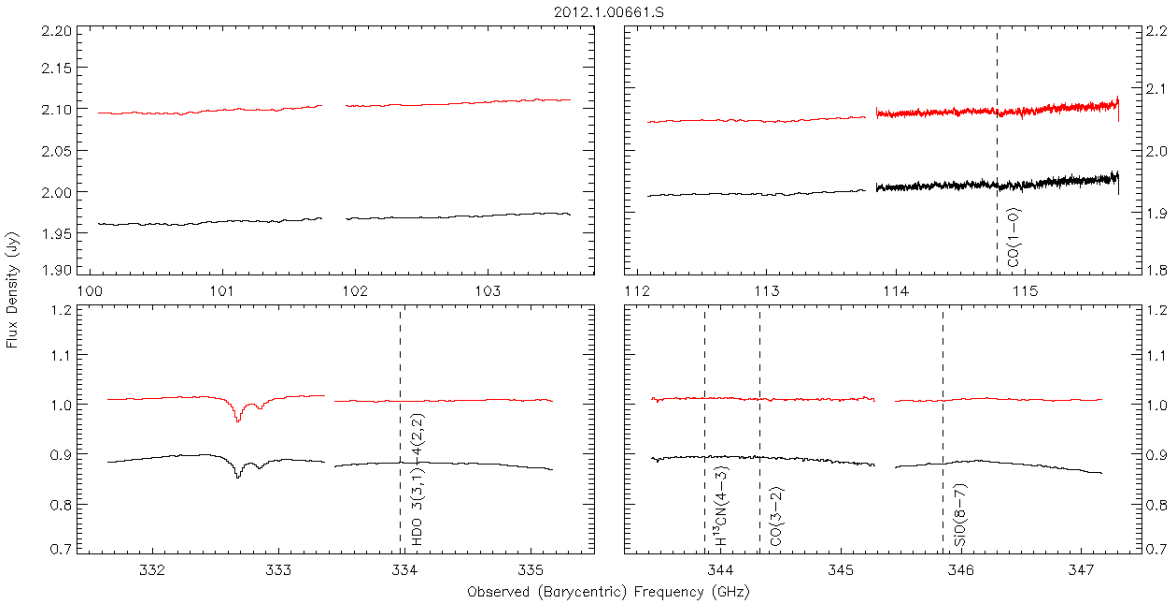

FIGURE 2.2: 2012.1.00661.S observations, Mar 7 (top) and Jan 28 (bottom). The continuum are integrated either over full beam shape (black) or at peak-intensity pixel (red). 7 Mar 2014 (top) and 28 Jan 2014 (bottom). The dashed lines represent the expected transition lines from M87 at z=0.00428 with type of transition labeled. Two features at ν=332.65 GHz and ν=332.8 GHz do not originate from M87. A mild but broad emission feature centers at 346.2 GHz and extends from $\sim$ 345.8 GHz to 346.4 GHz.

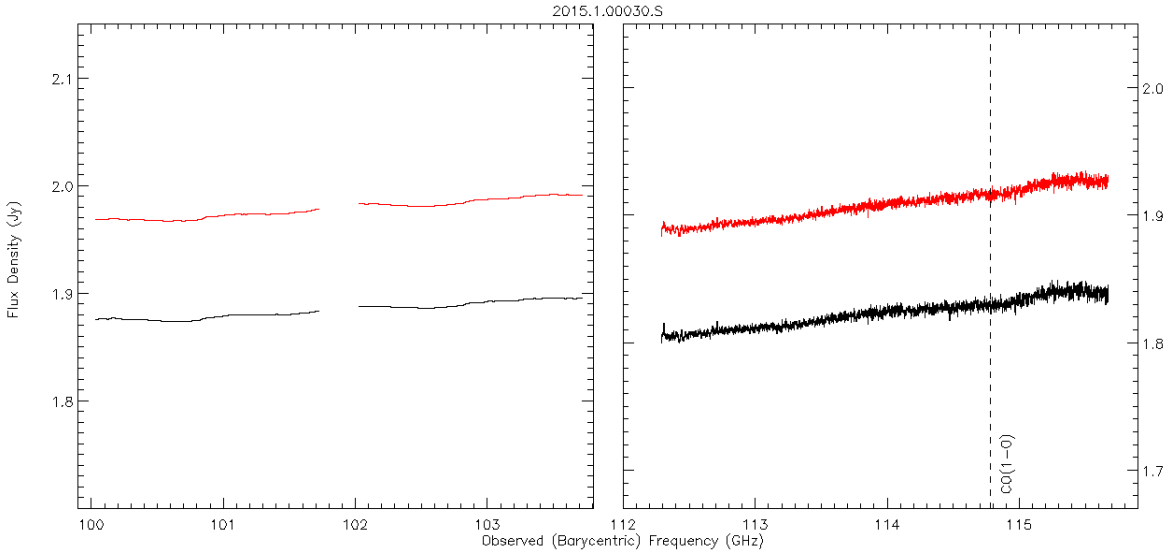

FIGURE 2.3: 2015.1.00030.S continuum, integrated over full beam shape (black) or at peak-intensity pixel (red). The dashed line represent the expected CO transition line from M87 at z=0.00428. The spectrum on the right is from two spectral windows combined together. Two mild broad diffuse emission features are present in the spectrum at $\sim$113.5-114.5 GHz and at$\sim$ 115-115.6 GHz.

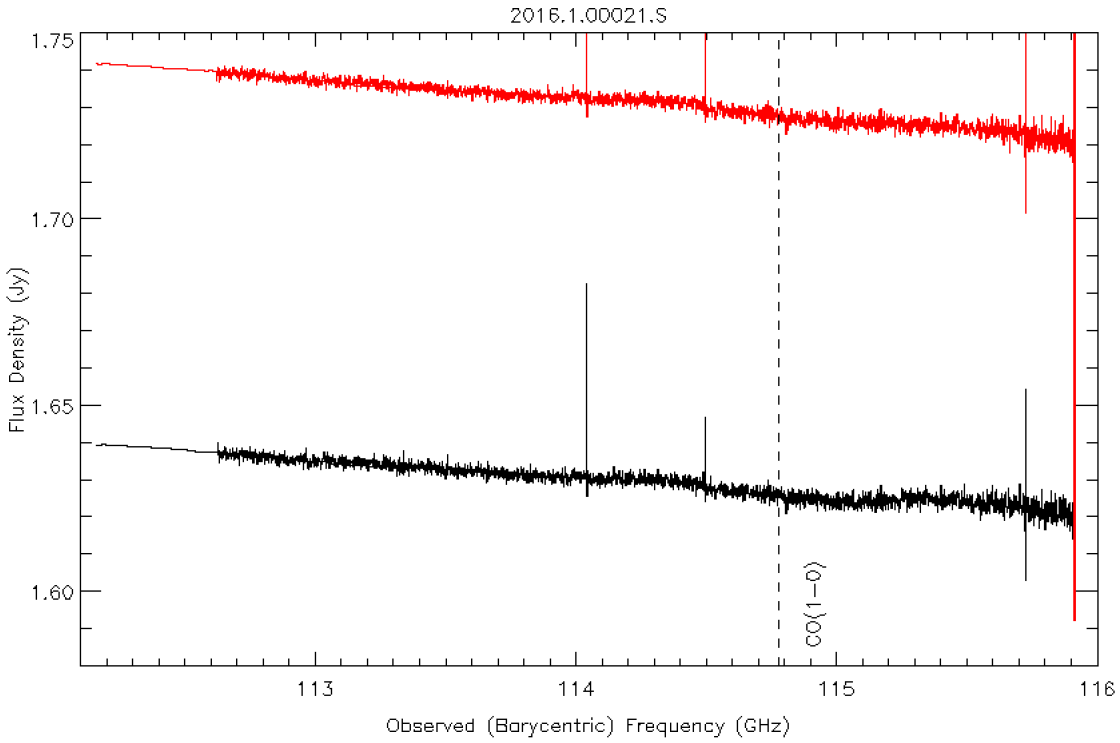

FIGURE 2.4: 2016.1.00021.S continuum, integrated over full beam shape (black) or at peak-intensity pixel (red). This spectrum is the result of combining 4 spectral windows from the 2016.1.00021.S observation. The dashed line represent the expected CO transition line from M87 at z=0.00428. We observe a small absorption feature at 114.81 GHz with a depth of 5 mJy and two mild broad diffuse emissions at ∼114.1-114.5 GHz and at∼ 115.2-115.9 GHz. Prominent sharp emission features are at the end or beginning of the spectral windows and are considered as signals from bad channels.

programs and a calibration issue when phasing all elements together into a single array, and not an intrinsic feature of the source. All three observations from program 2016.1.01154.V (Figure 2.6) have a small absorption feature of 0.3 Jy at 229.60 GHz, but the one in the last observation is almost consistent with the fluctuations in this spectrum. Two observations in program 2017.1.00841.V (Figure 2.7) both have a feature at 229.69 GHz, with a line depth of less than 0.2 Jy. The observation on Apr 20 (top) has a less noisy continuum which makes the feature easier to distinguish from its continuum, while the other observation (bottom) is noisier and thus harder to distinguish the feature from the fluctuations in its continuum.

The only measurement set that covers the CO(3−2) transition at 345 GHz is 2012.1.00661.S (28 Jan 2014; Figure 2.2; bottom). No obvious absorption of

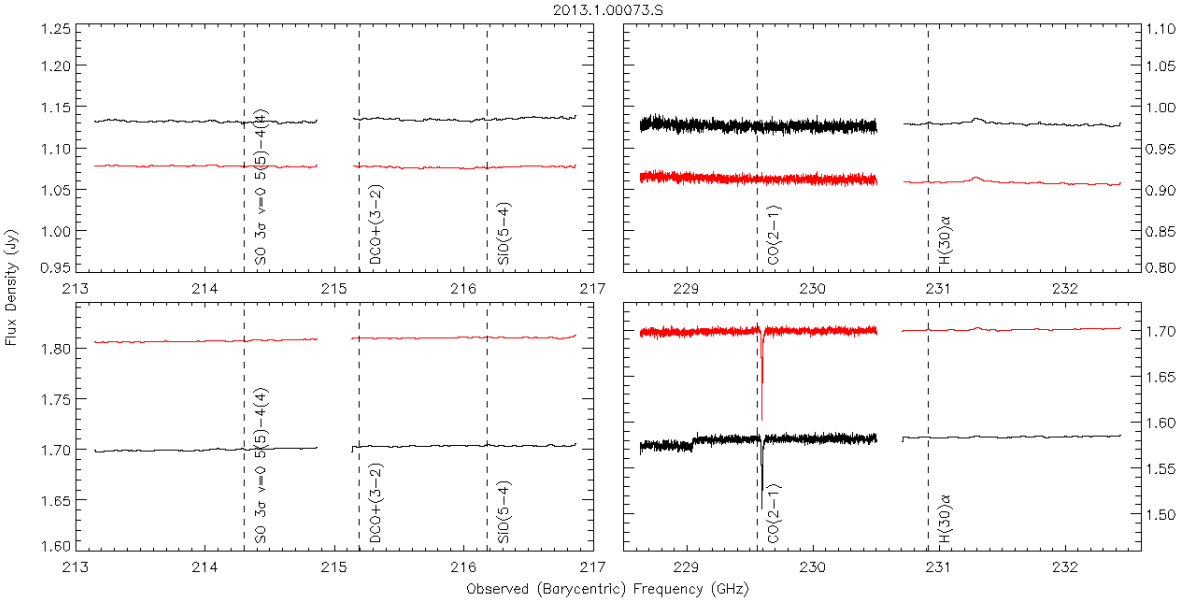

FIGURE 2.5: 2013.1.00073.S continuum, integrated over full beam shape (black) or at peak-intensity pixel (red). Observation Jun 14 (top) and observation Aug 16 (bottom) at the same frequency coverages across 4 different spectral windows. We observe an absorption line of 50 mJy at 229.60 GHz in Aug 16's observation, but not in the Jun 14's observation. This absorption line has a slight shift of 0.01 GHz from the frequency of redshifted CO(2−1) transition from M87.

CO(3−2) is present around 345 GHz, but two absorption features around 332.75 GHz are prominent. They are not close to any absorption features that could have originated from M87 and might be a local absorption feature from the Earth's atmosphere. It is possible that the column densities of gas in the Earth's atmosphere during observation were not consistent with the data used for calibration, thus these are examples of atmospheric absorption lines that were not properly removed in the data reduction process. Similar atmospheric absorption lines are also present around 215 GHz in all three observations in program 2016.1.01154.V (Figure 2.6) and in both observations in program 2017.1.00841.V (Figure 2.7). This brought up some re-thinking of the strong absorption line centered at 229.60 GHz in the Aug 16 observations in program 2013.1.00073 (Figure 2.5 (b)), as it is centered at the same frequency where the local $O_3(23-24)$ transition occurs.

The spectra of the other observations that are not mentioned in this section are listed in Appendix A. They either do not cover the frequencies we expect a CO transition to appear, or they do not show any apparent transition lines that could either be atmospheric transitions or CO transitions.

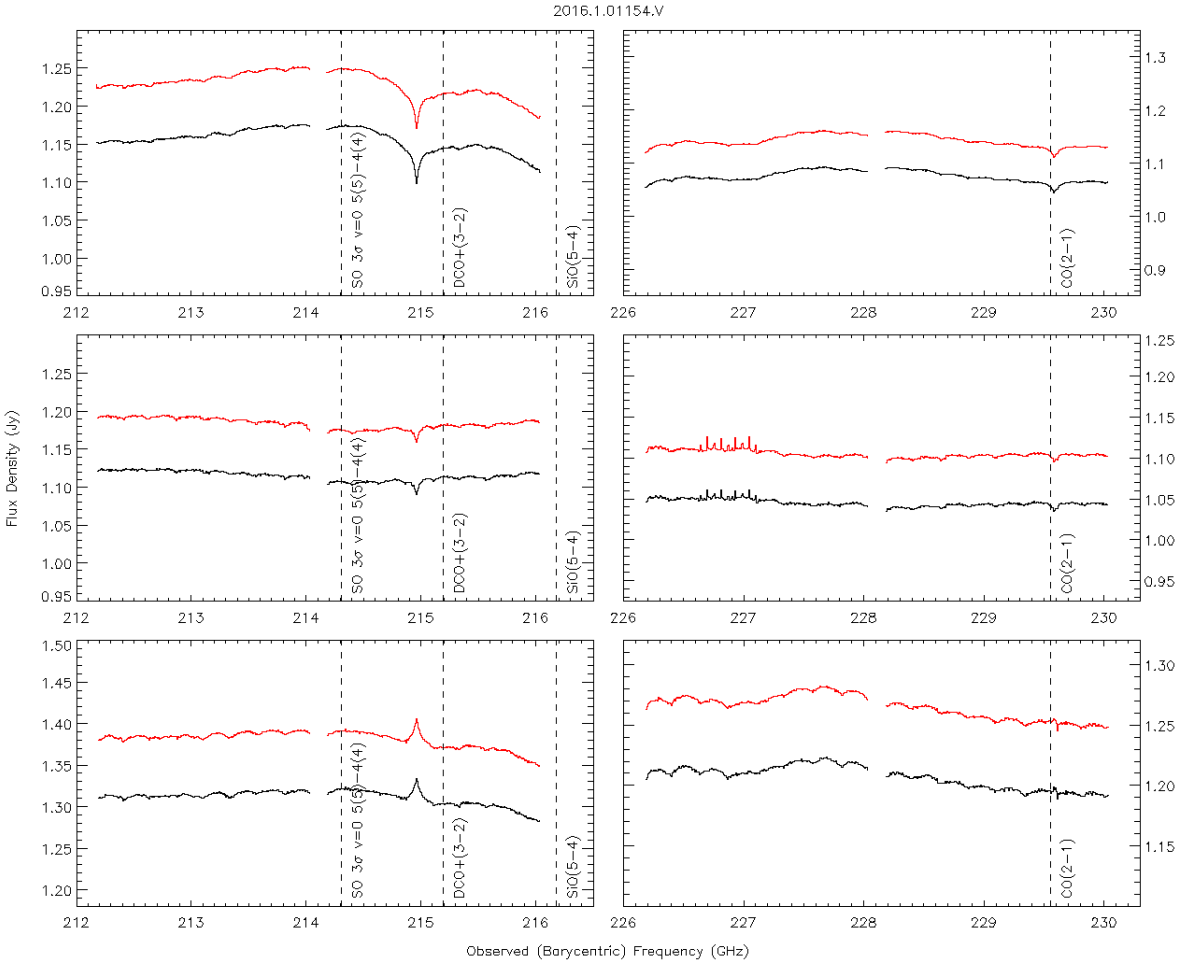

FIGURE 2.6: 2016.1.01154.V continuum, integrated over full beam shape (black) or at peak-intensity pixel (red). Observed on 5 Apr 2017 (top), 6 Apr 2017 (middle), 11 Apr 2017 (bottom) respectively. This is a project that involved global collaboration with Event Horizon Telescope (EHT). The fluctuations are due to some calibration issues with the .V programs. The features centered at 215 GHz have varying strength in each observation. It might be that the features in top two observations are under-corrected and the feature in the bottom one is over-corrected.

2.4 2013.1.00073 Phase Calibrator

While examining the abnormally sharp and deep absorption line at $\nu_{\rm sky} \sim 229.59$ GHz in 2013.1.00073.S Aug 16 (Figure 2.5 (bottom right)), we found that the phase calibrator for these observations, quasar J1229+0203, was flagged around 229.59 GHz (shown in Figure 2.9 (left)). These flags were added manually before

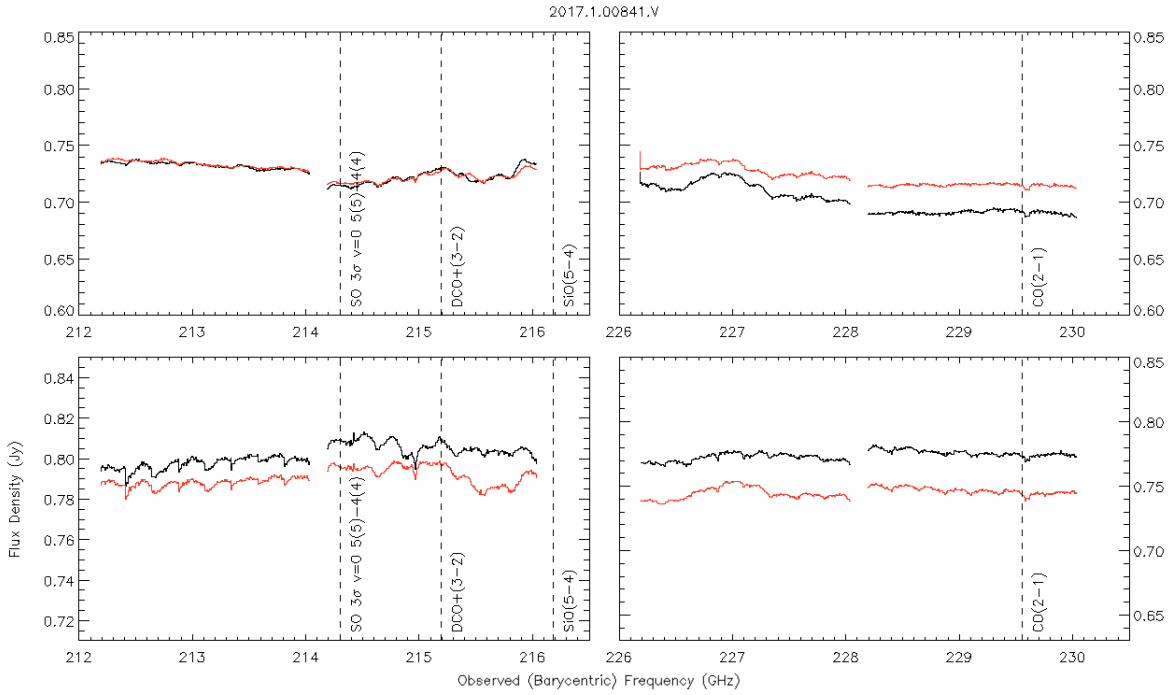

FIGURE 2.7: 2017.1.00841.V continuum, integrated over full beam shape (black) or at peak-intensity pixel (red). Observations from Apr 20 (top), Apr 21 (middle), and Apr 24 (bottom) These are noisy observations with the noise introduced from the calibration issues from .V programs. Although the features at 229.6 GHz are at the proper frequencies to be considered as real absorption from M87, they might be a mixture of both fluctuations in these .V programs and real absorption. We do not know if features are completely real, but we consider them to be in our analysis.

calibration and imaging by ALMA staff, although we do not notice any absorption features in that region after re-imaging J1129+0203. The M87 continuum of program 2013.1.00073 (Jun 14; Figure 2.5 (top two)), the other observation taken on a different date from the same project, is free of any features at 229.59 GHz. Its phase calibrator does not show any flags and is thus properly calibrated. Dr. Boizelle removed the flags around the frequency range corresponding to the absorption feature in J1229+0203 in Aug 16's observation and re-imaged M87. Figure 2.9 (b) presents the new image with a much weaker absorption line. We only see the deep absorption line with the flagged calibrator and the depth of the old absorption line, about 0.1 Jy, is about 10 times larger than that in the recalibrated data, about 0.01 Jy. There is not an obvious absorption line in the Jun 14 observations either. Thus we confirm that the flag in the calibrator of Aug 16's observation causes that absorption line to be abnormally strong and not properly

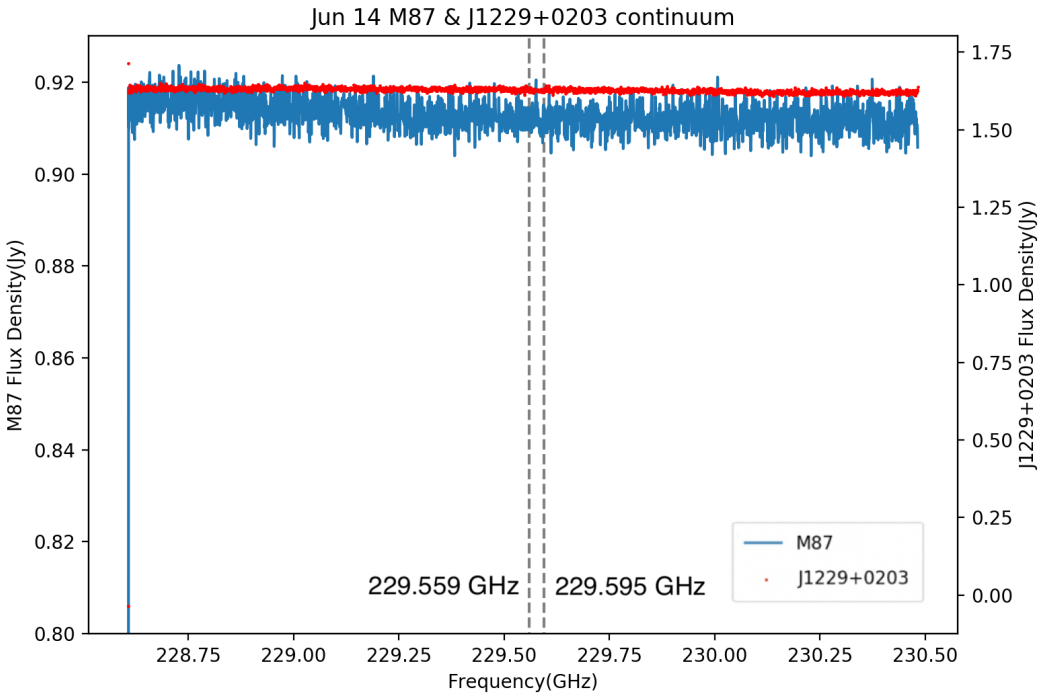

FIGURE 2.8: 2013.1.00073 14 Jun 2015 M87 & J1229+0203 Continuum at Peak-Intensity Pixel. No obvious absorption feature is present around 229.57 GHz, comparing to Figure 2.9 (left), the observation of the same program but from a different date and with a strong absorption feature of $\sim$ 0.1 Jy. The phase calibrator J1229+0203 does not have any flags and is continuous for this particular spectral window, except at the very beginning of the continuum. The huge drop in flux density at the beginning of this channel is caused by bad data point of the phase calibrator.

calibrated.

All the observations were cleaned, i.e., to reduce noise like atmospheric features, systematic noise, and radio frequency interference, before we retrieved them from ALMA archive. A bright source whose spectrum is well known and that is close to the target M87 on the sky is chosen for this data reduction process. Its spectrum is measured during the observation and compared to its well studied spectrum to build up a transmittance profile, which captures any atmospheric transitions during the observation. This transmittance profile is used to correct the spectrum of M87 and remove any identified absorption feature based on the transmittance profile. Thus the flagging region in the bandpass calibrator, J1229+0203, caused the absorption feature in M87 to be linearly interpolated and not correctly cleaned.

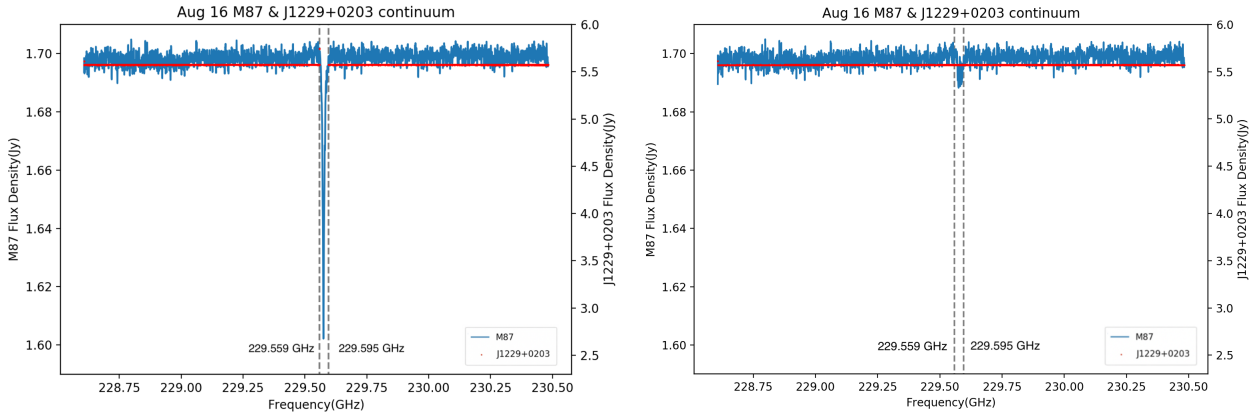

FIGURE 2.9: 2013.1.00073 Aug 16 peak-intensity pixel continuum. Figure on the left is the old spectrum with the flags in 229.559–229.595 GHz and a strong absorption feature of 0.1 Jy in strength. Figure 2.8, the other observation from Jun 14, does not show any obvious absorption feature at the same frequency range. Its phase calibrator has a continuous spectrum. Figure on the right is the new spectrum after we removed the flags in the calibrator and re-imaged M87. The new spectrum has a weaker absorption line, with a depth of only 0.01 Jy.

2.5 Atmospheric Modeling

The presence of residual atmospheric absorption after data reduction led us to rethink the treatment of these features and how that would affect our absorption line analysis, especially with the strong absorption line at 229.60 GHz in program 2013.1.00073.S (Figure 2.5). We used the atmospheric modeling tool `am`, developed by Smithsonian Astrophysics Observatory (SMA; Paine 2019), to calculate the transmittance profile in the atmosphere and estimate how much these atmospheric absorption lines would affect our line studies. The model is defined with multiple horizontal atmosphere layers along the line of sight. Each layer can have input parameters like pressure, temperature, column densities of certain molecules, water vapor, etc. The program performs radiative transfer calculations for slight lines through the layers. This determines how much radiation at a specific frequency, ν, propagates through a modeled atmosphere, with the equation

$$I_i(\nu) = B(\nu, T_i) \cdot (1 - e^{-\tau_i(\nu)}) + I_{i-1}(\nu) \cdot e^{-\tau_i(\nu)} \tag{2.1}$$

where $I_i(\nu)$ is the radiance at the lower boundary of the i^{th} layer, $\tau_i(\nu)$ is the total opacity of the layer, and $B(\nu, T)$, the Planck radiance function, is defined as

$$B(\tau, T) = \frac{2h\nu^3}{c^2 \cdot (e^{\frac{h\nu}{kT}} - 1)} \ . \tag{2.2}$$

This step is repeated for all layers defined in the model along line of sight until the bottom layer is reached. Combining all the radiation transferred with the initial radiance entering the first layer gives the the output radiance at the bottom layer of the model.

The `am` cookbook gives a defined realistic model for the atmosphere above Mauna Kea, Hawaii, based on their study of the atmosphere over ten years. There are 29 layers of atmosphere in this model with pressure and temperature defined at the base for each layer. The gas columns defined are water vapor and ozone, which is sufficient for analysis in the band coverage of our MS, as we did not see any other prominent transitions present in the frequency ranges we are interested in. Since Mauna Kea is at an altitude close to ALMA, we took this well-defined model to calculate an approximate transmittance profile above the Atacama desert. Inputs like zenith angle, ground-level temperature, and precipitable water vapor (PWV) were adjusted according to each observation. PWVs for all the observations are listed in Table 2.1. Altitudes of each observation in degrees and ground-level temperature in degrees Celsius are listed in Table 2.2. The binning of the transmittance profile was adjusted to match the binning of each spectral window. This captures the absorption features at the same spectral resolution so that they will be comparable to the features in our observation.

We plot the general transmittance profile in Figure 2.10 to provide an overview of the ALMA Band 3, Band 6, and Band 7 frequency ranges, which cover the three CO transitions we are interested in. The binning is adjusted for display purposes, 10 MHz for both Band 3 and Band 6 and 50 MHz for Band 7. The overall shape of the transmittance profile is almost linear with some major drops at 115 GHz and around 325 GHz. These drops are due to the significant amount of water vapor present in the atmosphere. Band 3 (Figure 2.10 (top left)) drops about 20% from 110 GHz to 115 GHz, which means the spectrum within that range including CO(1−0) transition at 114.78 GHz, may have a drop in flux density in

Project Code	**Elevation (deg.)**	**Ground Temperature(°C)**
2012.1.00661.S Mar 7	44	1
2012.1.00661.S Jan 28	49	1
2013.1.00073.S Aug 16	54	−7
2013.1.01022.S	48	1
2015.1.00030.S	50	−4
2015.1.01170.S	50	1
2015.1.01352.S Oct 25	52	2
2015.1.01352.S Oct 31	52	3
2016.1.00021.S	48	−2
2016.1.01154.V	44	−7
2017.1.00608.S	45	0

TABLE 2.2: Average elevations and ground level temperatures for each observing block and are used to calculate atmospheric transmission profiles.

its continuum. Band 6 (Figure 2.10 (top right)) has a minor change in the overall transmittance, but there are some atmospheric absorption lines present between 230 GHz to 240 GHz. This could affect the CO(2−1) spectra if these atmospheric effects were not fully removed during calibration. Band 7 (Figure 2.10 (bottom left)) also has atmospheric absorption lines at around 335 GHz which is in the observation window that covers CO(3−2) transition.

We also looked for any atmospheric features at the same frequencies as the observed absorption lines we identified as CO transitions. Figure 2.11, Figure 2.12, and Figure 2.13 are the three identified CO(1−0) transitions compared to `am` results. We plotted our results with flux densities being the primary y-axis on the left hand side and transmittance profile being the secondary y-axis on the right-hand side. The scale of both y-axes were adjusted so that both axes would show comparable drop in percentage. The `am` results show an atmospheric $O_3(23-24)$ transition with a drop of 0.5% at 114.98 GHz. Both programs 2012.1.00661 and 2015.1.00030 show an absorption feature of 0.01 Jy that match with the atmospheric ozone feature. These absorption features have roughly 0.5% drop in flux densities which matches with the 0.5% decrease in the transmittance profile of the `am` model. These are evidence that the atmospheric features are not completely removed the these observations. Program 2016.1.00021 does not show any significant drop at the same frequency, so it is a better calibrated observation compared to the other two in this frequency range.

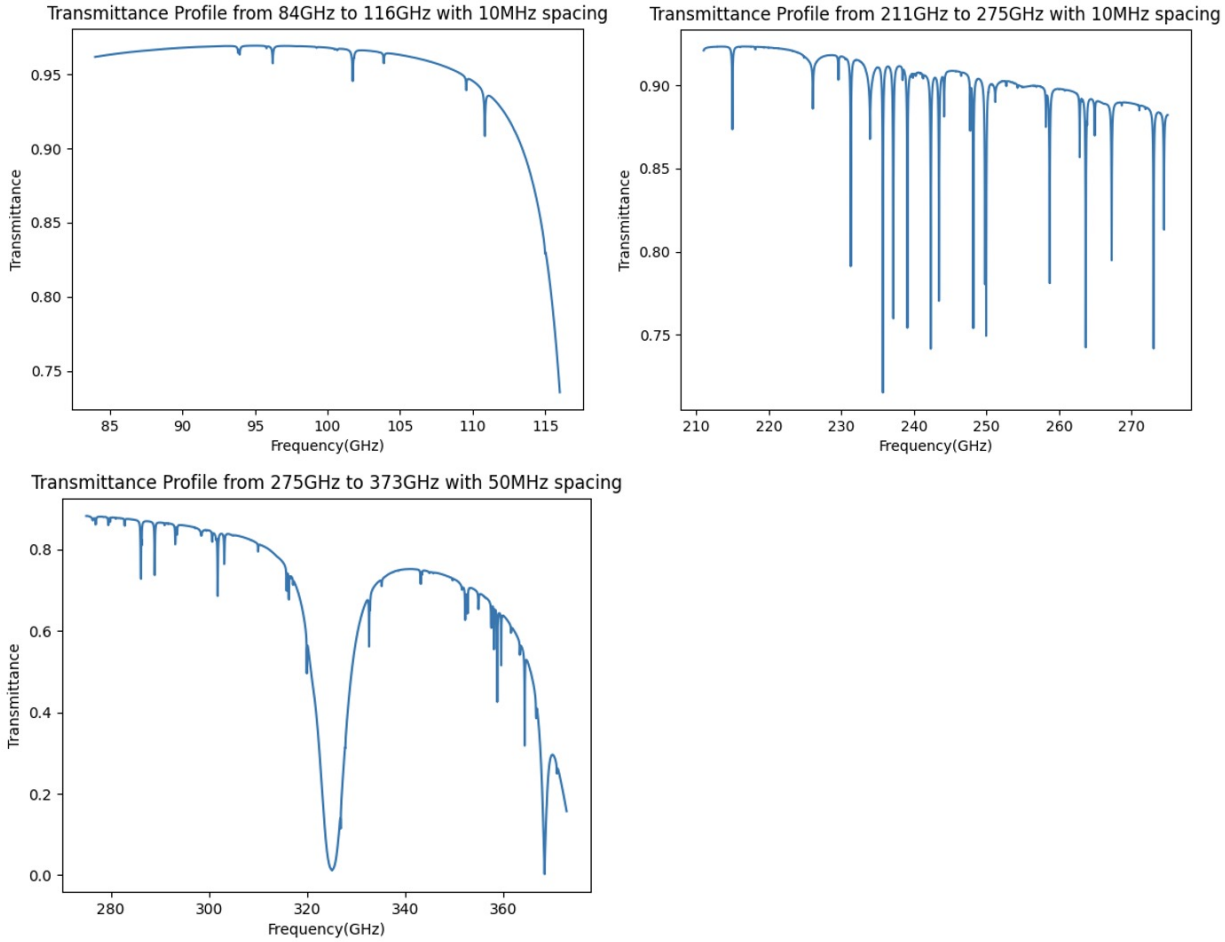

FIGURE 2.10: Atmospheric transmission profile from am for each ALMA band. Band 3 (top left) covers 84 GHz−116 GHz. Band 6 (top right) covers 221 GHz−275 GHz. Band 7 (bottom left) covers 275 GHz−373 GHz. Huge drops at 115 GHz and 320 GHz are typically due to water vapor, the the other absorption lines are due to other gases like ozone. Absorption lines, for instance, the two at $\sim$ 110 GHz, and a few close to $\sim$ 235 GHz, lie in the spectral windows of our observation. Details are provided later when the features in each particular spectral window are discussed.

With these `am` results, we are able to identify absorption lines that do not originate from M87 but were due to local atmospheric transitions and were either under- or over-corrected in the data reduction. Figure 2.14 shows evidence of residual atmospheric absorption in the Jan 28 observations of program 2012.1.00661. The peaks of two ozone transition lines at 332.70 GHz and 332.88 GHz in the transmittance profile match with the peaks of two transition lines in the continuum of the observation. The `am` transmission profile shows the O_3 absorption line at 332.70 GHz drops for 15% and the other absorption line at 332.88 GHz drops for

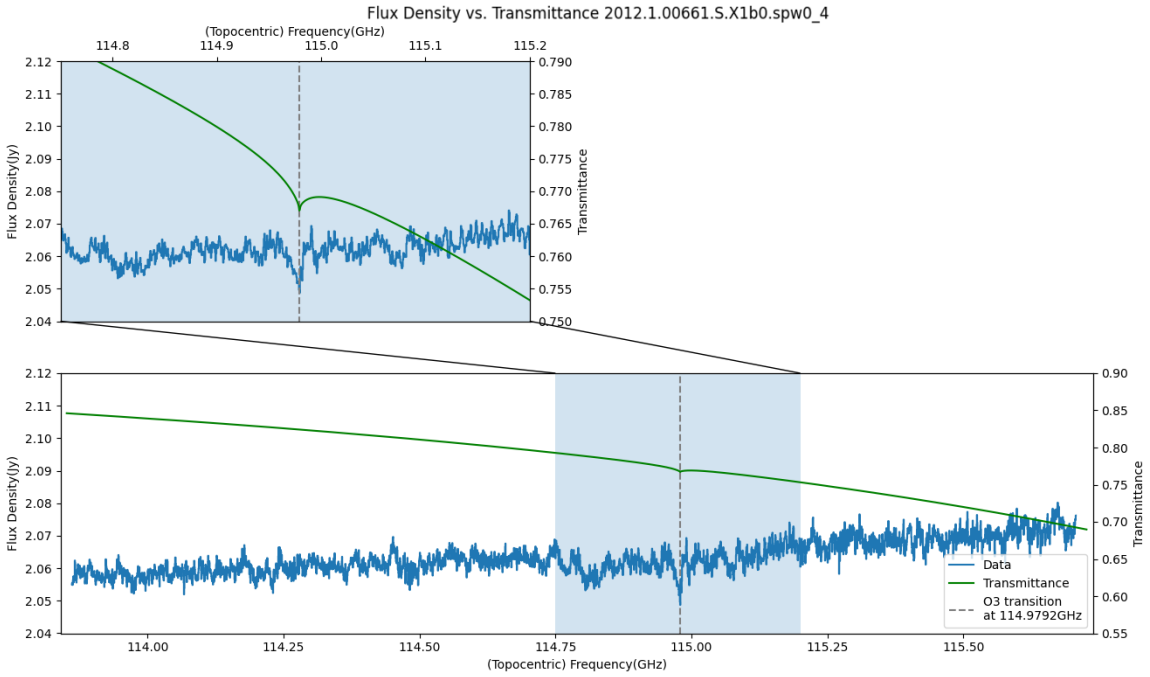

FIGURE 2.11: Peak-intensity-pixel flux density from 2012.1.00661.S Mar 7. The observed transition with a line strength of ~ 0.01 Jy at 114.98 GHz corresponds to rest frame $O_3(5-6)$ transition, which causes 5% drop in transmittance. This feature is visually slightly larger than the noise in the continuum. If we consider this absorption line is an absorption feature and not systematic noise, this line can be explained by the O_3 transition at 114.98 GHz. Thus this line is an atmospheric transition line, not an absorption line originated from M87.

5% in transmittance. The two observed features show drops in flux density of less than 2.5%. The depth of the observed features does not match with `am` results, thus these features are corrected to some extent but not fully corrected in the data reduction. It is altogether likely that O_3 column densities differed slightly between the target and the bandpass calibrator, meaning that the data reduction process would not perfectly correct for the actual ozone layer along the target's line of sight.

Multiple reasons could contribute to the insufficient calibration in removing the atmospheric features. One could be that although J1229+0203 is close to M87 on the sky, they are still separated by some distance. Slewing from M87 to J1229+0203 would cause ALMA to look at targets along different line of sights. They could have slightly different gas column densities along line of sights and thus inaccurate

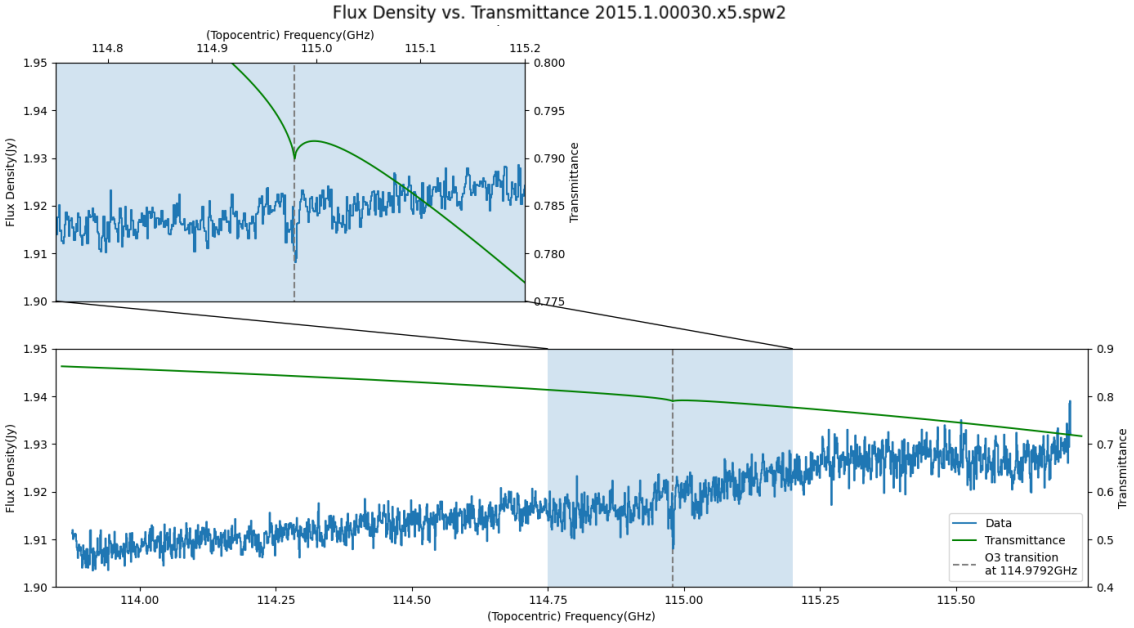

FIGURE 2.12: Peak-intensity-pixel flux density from 2015.1.00030.S. The drop in flux density of 0.01 Jy at $\sim$ 114.96 GHz in the observed spectrum agrees with the O_3(23-24) transition at 229.57 GHz in transmittance profile. This feature is visually slightly larger than the noise in the continuum. If we consider this absorption line is an absorption feature and not systematic noise, this line can be explained by the O_3 transition at 114.98 GHz. Thus this line is an atmospheric transition line, not an absorption line originated from M87.

model of describing the atmospheric transitions.

Figure 2.15 shows the two observed features at 214.96 GHz and at 229.57 GHz and how they match with the atmospheric absorption lines at the same frequencies from `am` results. Thus with our `am` results, we confirm that these observed absorption lines are residuals of atmospheric features from data reduction. If the features were correctly predicted and removed during data reduction, then the spectra should be free of any atmospheric absorption features at these frequencies. However, there are different amounts of residuals present in these observations. The depth of the observed lines varies across the three observations with the observation on Apr 6 (middle) having the smallest residuals. Both observations from Apr 5 (top) and Apr 6 (middle) are under-corrected, with the features still remain negative compared to the continuum. The observation from Apr 11 (bottom) is over-corrected, as the ozone feature becomes positive with respect to the continuum.

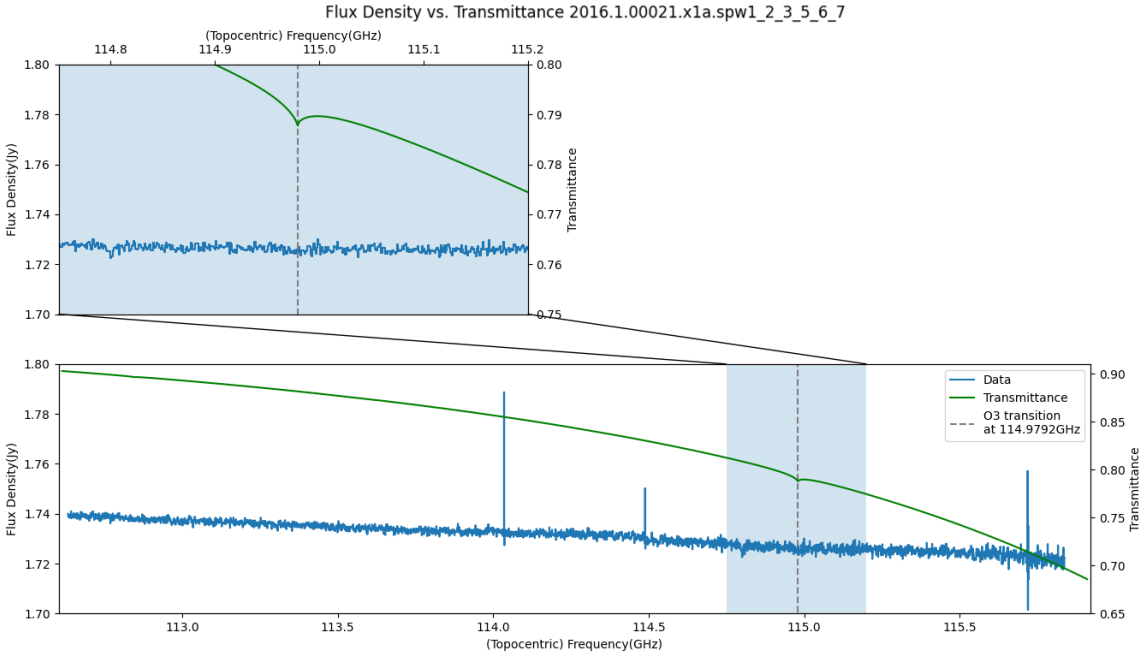

FIGURE 2.13: Peak-intensity-pixel flux density from 2016.1.00021.S. We do not see any apparent absorption feature in the observed spectrum, which means this observation is better calibrated compared to previous observations with atmospheric absorption lines.

Even within the same program, observations on different dates would still have variations in the atmospheric absorption features after data reduction.

Figure 2.16 shows the old strong CO(2−1) absorption feature at 229.57 GHz from program 2013.1.00073 (Aug 16). It matches with $O_3(23-24)$ transition at 220.575 GHz. Based on our model, the atmospheric transition only accounts for a 2% drop in transmittance, but the observed absorption line has a 4% drop in flux density. If half of the observed absorption line is due to the 2% drop in transmittance predicted by the atmospheric absorption, we can consider the other half to be real CO(2−1) absorption from M87, as we do not have any other sources that can cause an absorption line in this particular frequency. So even if this observed absorption feature is considered to be improperly calibrated, we can decompose the feature into both atmospheric absorption and absorption from source of interest, as is done in Section 3.2.3.

Figure 2.17 shows the new CO(2−1) absorption feature after we removed the flag in the phase calibrator and corrected the spectrum. The 0.75% decrease in flux

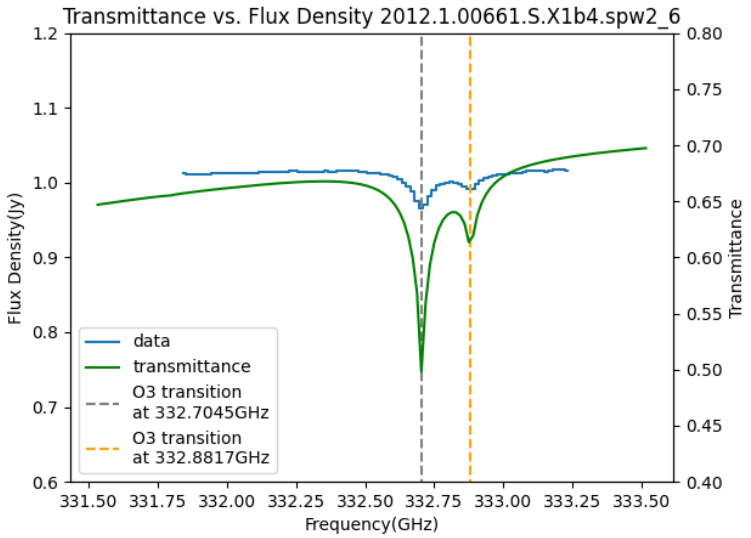

FIGURE 2.14: Central flux density from program 2012.1.00661.S.x1b0. The feature at 332.7045 GHz corresponds to O_3(11(2,10)-11(1,11)) transition, and the one at 332.8817 GHz corresponds to O_3(2(2,0)- 1(1,1)) transition. The centroids of observed features in the M87 spectrum agree with the centroids of the drop in transmittance profile, thus we consider these features to be atmospheric absorption. The strengths of observed features do not match with the strength of the features in the transmittance profile. This might mean that these observed features are partially reduced from general calibration. It could also be because of model we used in producing the transmittance profile is the atmosphere above Mauna Kea, not the atmosphere above ALMA. The transmittance profile we produced might not describe the atmosphere along line of sight above ALMA accurately.

density of the observed absorption line is less than half of the 2% decrease in transmittance. It might be that the atmospheric feature is partially calibrated, still with some residuals in the spectrum, as we do not see any absorption features in Jun 14 observation.

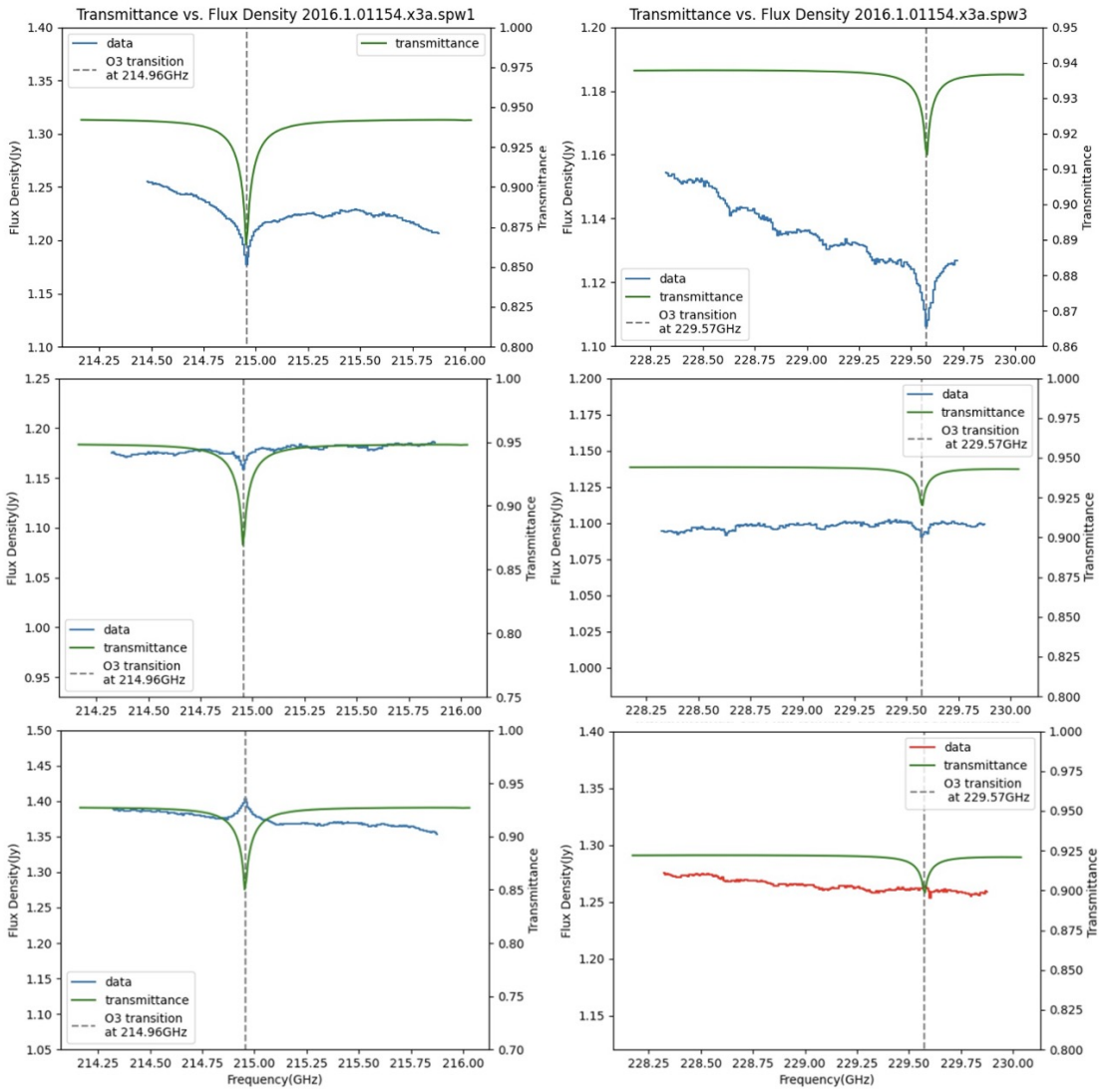

FIGURE 2.15: Central flux density from program 2016.1.01154.V. Observations from Apr 5 (top), Apr 6 (middle), Apr 11 (bottom) These three observations have the same band coverage and thus the same features are identified. The first column presents the continuum in spw 1 and the second one presents the continuum in spw 3. The absorption features in program 2016.1.01154.xc in the third row are positive. It is likely that there is over-correction for atmospheric absorption during the calibration process of these observations.

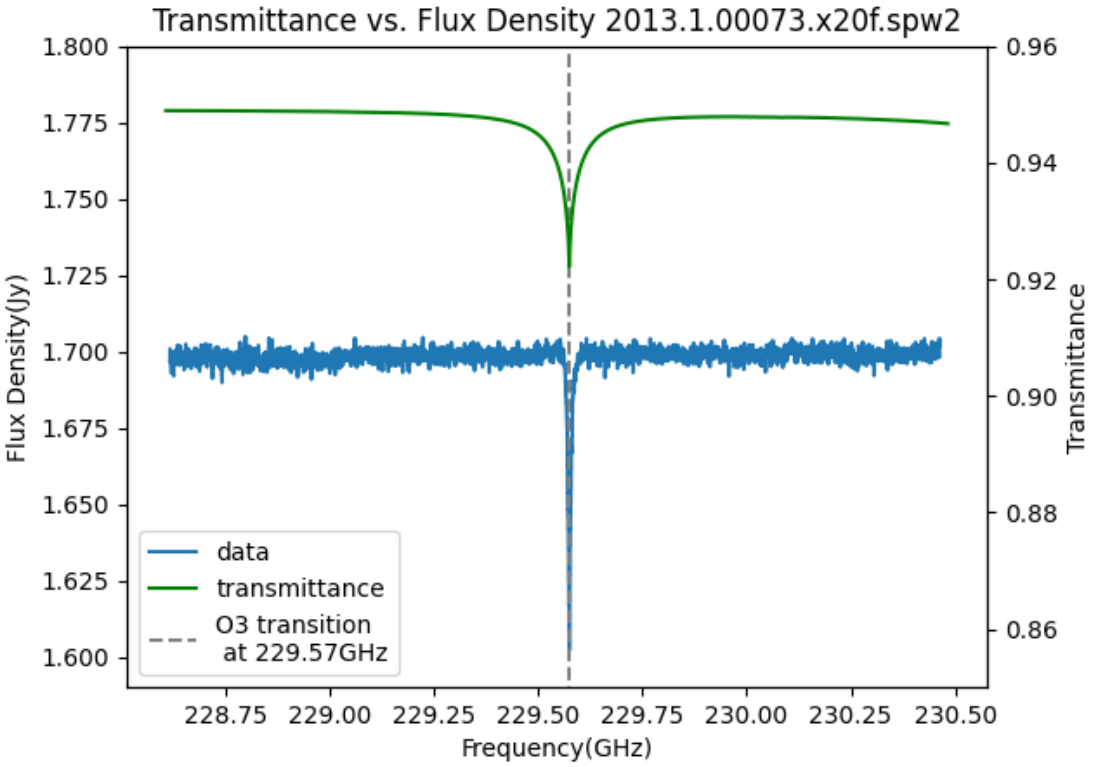

FIGURE 2.16: Old continuum from observation 2013.1.00073.S Aug 16 calibrated with flags in its calibrator J1229+0203. The centroid frequency of the sharp absorption line with a line strength of 0.1 Jy agrees with the the centroid frequency of $O_3(23-24)$ transition at 229.5750 GHz.

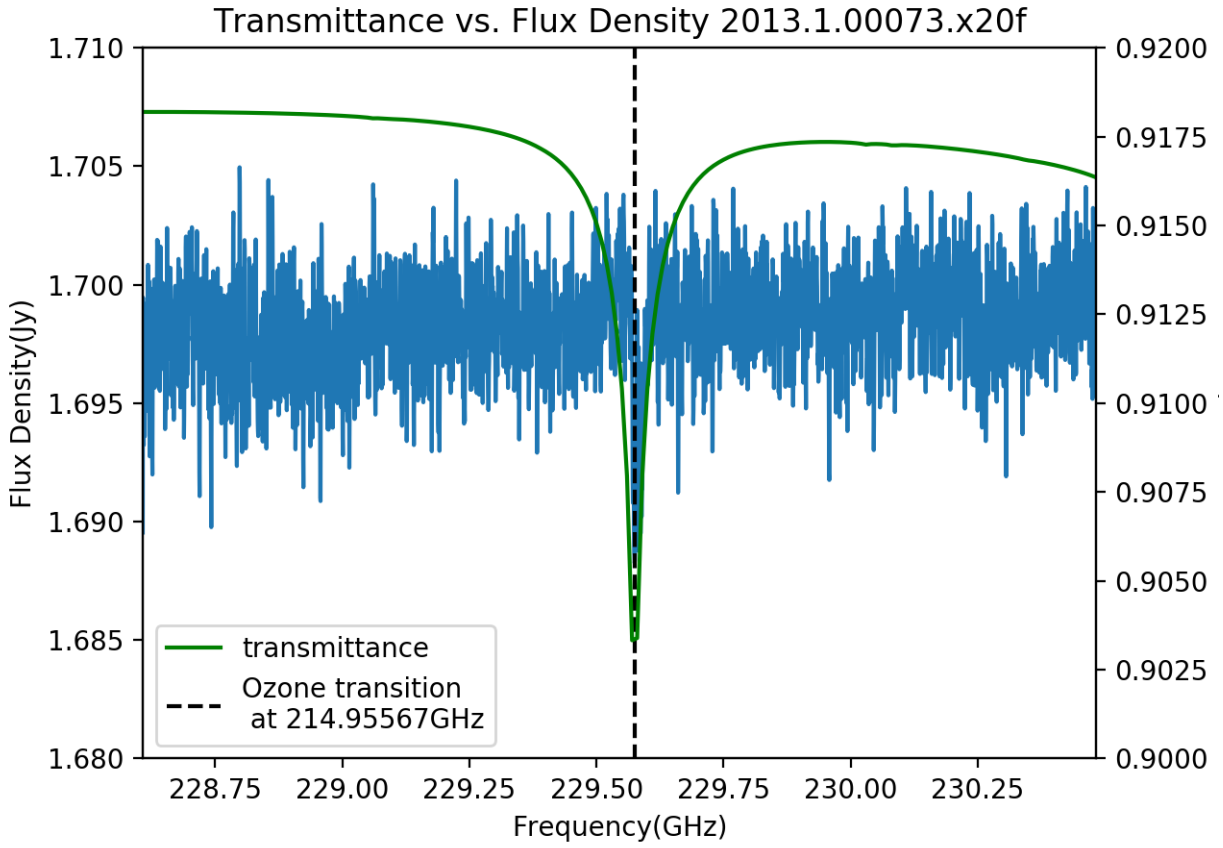

FIGURE 2.17: New continuum from program 2013.1.00073 (Aug 16), with the flags in phase calibrator around 229.57 GHz removed. The new feature of 0.015 Jy(0.8%) is more comparable with the drop of 0.15% in transmittance profile.

CHAPTER 3: Measurement Techniques

We have identified a few absorption lines and two pairs of emission features. Although we do not know if there are any atmospheric transition line residual present in these features, we base our analyses in this section on the assumption that they originate completely from the gas clouds in M87, not from the Earth's atmosphere. With this assumption, we were able to study the Hydrogen column densities and gas kinematics of M87. We present our methodologies and derivations in this section.

3.1 Peak Frequency Ratio Test

We first verified if these lines are at the expected frequencies of redshifted CO line transitions via ratio test. It is possible to calculate the redshift of these lines which would be compared to the redshift of M87, but it is possible that the gas has a relative motion with respect to M87. Instead, we used a ratio test, which eliminates the effect of redshift but still can verify the validity of the observed lines. The relationship between redshift z, emitted or rest frequency $\nu_{\rm emit}$, and observed frequency $\nu_{\rm obs}$, due to non-relativistic Doppler shift, is:

$$z \equiv \frac{\nu_{\rm emit} - \nu_{\rm obs}}{\nu_{\rm obs}} \tag{3.1}$$

or:

$$\nu_{\rm obs} = \frac{\nu_{\rm emit}}{1+z} \tag{3.2}$$

Often, absorption or emission lines arising from gas that is bound to a galaxy will be found at the same *average* $\nu_{\rm obs}$ as the average stellar motion of the galaxy. However, the motion of gas near the central BH does not always agree with that of the host galaxy for two primary reasons. (1) It is possible that the gas is not in perfect circular motion, as in the case of inflowing or outflowing clouds. This motion with respect to the center of M87 may introduce a relative velocity component in the radial direction. Thus simply comparing the frequencies of

observed features to expected frequencies of transition lines at the redshift of M87, which is $z = 0.00428$, is not always sufficient for verification in the case of faint or ambiguous line detection. (2) Discrete gas clouds, especially those seen in absorption, may have different motion than the average gas kinematics. If the motion is in radial direction, then the redshift of the gas will be different from the recessional velocity of the system. Thus the observed frequency will deviate from the frequency where the transition line should occur based on the galaxy's redshift.

For a single gas cloud with a consistent z, taking the ratio of two observed frequencies eliminates the redshift term, making this ratio comparable to the ratio of rest frame frequencies:

$$\frac{\nu_{\text{obs1}}}{\nu_{\text{obs2}}} = \frac{\nu_{\text{emit1}}/(1+z)}{\nu_{\text{emit2}}/(1+z)} = \frac{\nu_{\text{emit1}}}{\nu_{\text{emit2}}}. \tag{3.3}$$

This comparison can be used as a preliminary test to verify that observed absorption and emission features are at appropriate frequencies, giving stronger confidence in low S/N detections.

Results and discussions are demonstrated in Section 4.1.

3.2 Model Fitting

3.2.1 General single-Gaussian model

We want to study the line characteristics, i.e., the centroids and the height, of these transition lines. These characteristics and be used to estimate and study the gas kinematics of M87. We first assume the absorption features identified are completely real absorption features originating from M87. In keeping with other studies (e.g. Rose et al. 2020), we modeled the identified line features using Gaussian functions. The continuum is generally flat and can be considered as a linear function with some noise. Thus the model for the fitting has at least two components: a linear function fitting the continuum and one or more Gaussian functions fitting the absorption.

The `Python` function `least_squares` from the package `scipy.optimize` was used for fitting. Based on the initial parameters, it minimizes the sum of the differences between the model and the data to get the best-fit parameters. The parameters can be restricted with upper and lower bounds to avoid spurious results.

We first define our model's parameters. The linear part of the model is defined as

$$F = m\nu + b \ , \tag{3.4}$$

with m being the slope, b being the y-intercept, F being the flux densities from the spectrum, and ν being the frequency. The model including the Gaussian function is defined as

$$F = ae^{-\frac{(\nu-\nu_0)^2}{2c^2}} + m\nu + b \ , \tag{3.5}$$

where a is the height of the absorption line in Jy, ν_0 is the centroid of the Gaussian function in GHz, and c is the standard deviation in GHz.

We then fit all continuum spectra with the linear function. The linear fitting region was selected in a way that any absorption or emission features were excluded. For programs like 2016.1.01154.V (Figure 2.6) and 2017.1.00841.V (Figure 2.7), which contain the oscillating fluctuations in continuum, instead of intentionally selecting a shorter and more linear-looking region, we included as much continuum as possible to capture the overall increasing or decreasing trend of the spectrum.

After optimizing the linear fit, we refit all the spectra with an identified absorption feature about the CO frequency using the Gaussian function model. The initial linear parameters are set to be the results of best-fit linear parameters. Sometimes `least_squares` returns final parameters that yields better reduced chi-squared but deviates from the large-frequency shape of the continuum. To get a final result that best describes the shape rather than the statistically best result, we explored setting restrictions on the final best-fit parameters. In a few cases where the Gaussian function does not connect with the linear function, we fixed the linear parameters to their initial best-fit values in the model to make sure the Gaussian function sits on the continuum. The centroids of the absorption features are also constrained to be below a maximum σ to make sure it is fitting to the correct Gaussian feature.

`least_squares` does not calculate the sum of systematic and random uncertainties, or the error budgets, of these parameters. Future work inspecting uncertainties will be given in Chapter 5.

We adopted a similar fitting routine as the single Gaussian model to fit the symmetric broad emission features in 2015.1.00030.S, 2016.1.00021.S, and the single broad emission feature presented in 2012.1.00661.S Jan 28. Each distinct emission feature is considered as a single Gaussian function, whose peak frequency in GHz, height in Jy, and width in GHz are calculated by `least_squares`. The peak frequencies and the widths of Gaussian fit are used to estimate the dynamics of the CO gas in M87 in Section 4.4.

We present the final best-fit parameters for each observation in Table 4.1 and a detailed discussion of our results in Section 4.2.

3.2.2 Decomposing the 2013.1.00073.S Aug 16 absorption line – multi-Gaussian real absorption components

Still assuming the abnormally strong absorption in program 2013.1.00073.S is completely real, there is a noticeable asymmetry in its shape close to the continuum on the right end, as shown in Figure 2.5. Other ALMA programs have identified similar asymmetries as arising from multiple gas components with intrinsically Gaussian absorption shapes but different column densities and line-of-sight velocities (e.g., Rose et al. 2020). If we consider the putative absorption feature in M87 to be made of multiple Gaussian components, then these components might be due to the intrinsic structure of the clouds. To decompose the different components of the absorption feature, we decompose this absorption feature with 1-Gaussian model, 2-Gaussian model, and 3-Gaussian model components. These models are the same as described in Section 3.2.1, except adjusting the number of Gaussian functions.

To determine how many Gaussian functions are sufficient to reproduce this feature, we calculated the reduced chi-squared $\chi^2_{\rm dof}$ value,

$$\chi^2_{\rm dof} = \frac{1}{N_{\rm dof}} \sum_i^N \frac{(O_i - F_i)^2}{\sigma_i^2} \tag{3.6}$$

where O_i and F_i are the i^{th} data and model flux densities, respectively. Noise per channel σ_i is estimated by the rms of the residual spectrum after the linear model fit. The degrees of freedom $N_{\rm dof}$ is equal to N channels minus the number of free parameters. The N channels only cover the region about redshifted CO transition, generally spanning perhaps as much as a few $\times$10 MHz.

We present the results of the multi-Gaussian models and their evaluation in Section 4.2.1.

3.2.3 Decomposing the 2013.1.00073.S Aug 16 absorption line – real absorption from M87 and atmospheric absorption residual

The transmittance profile close to 229.59 GHz (Figure 2.10) in Section 2.5 shows that it is possible that a portion of this absorption line (Figure 2.5) is due to atmospheric ozone. Even if the absorption feature in this initial MS was considered improperly calibrated, we want to use this line to discover a method for decomposing a line when the transition line from a source of interest overlaps with an atmospheric transition. We adopted two new models to account for both real CO absorption against the M87 nuclear continuum and a drop in transmittance in atmosphere. These two models both have a linear function describing the continuum and two Gaussian functions added together to describe the absorption feature. `least_squares` from Python `scipy` package is used to optimize the model and yield best-fit results. These two models adopt different restraints on the parameters optimized by `least_squares`.

The first model fixed the position of the peak of one Gaussian function to be the same percentage drop in transmittance based on the `am` model determined

in Figure 2.10 in Section 2.5. The transmittance profile showed a roughly 2% drop, thus the flux of the peak would be roughly 2% lower than the flux of the continuum at 1.656 Jy. The frequency of the peak is constrained to be in the range of 229.56−229.58 GHz, which covers most of the absorption feature. The width does not have any limits and is left as a free variable. We adopted this model because . But whether the features were completely corrected is unknown. Through this model we are able to correct for the atmospheric absorption residual present in the core area of this observed absorption line.

The second model fixed the width and the position of the centroids of the feature in transmittance profile, but left the height of the Gaussian function to be a variable that can vary freely to yield the best-fit result. We adopted the shape of the O_3 transmittance profile we got from previous `am` modeling results. Although we do not know the exact column density of ozone above ALMA, the transmittance profile still characterizes the atmospheric feature. We fixed the shape of the atmospheric absorption to match that of ozone absorption. As the strength in this line is determined by the column density of ozone, this model adjusts for the uncertainty in ozone column density along the line of sight to yield best-fit results. The CO(2−1) feature was modeled as a free-varying Gaussian function to add up to the rest of the observed feature.

We present the plots and numerical results of these two models along with some discussion in Section 4.2.2.

3.3 Absorption Lines

The high sensitivity of ALMA at mm/sub-mm wavelengths facilitates an unprecedented survey of molecular gas in galactic nuclei. In nearly all cases, CO absorption features are most likely molecular lines observed against bright continuum emission. In M87, the observed CO absorption enables the first ever study of molecular gas densities near the central BH. In this section, we detail the method used to calculate the column density of molecular hydrogen gas along the line of sight via the absorption line strength.

The integrated area of the absorption feature (underneath the interpolated continuum) is generally denoted as $W_{\rm CO}$. Using `Python` code I developed for this task, we measured $W_{\rm CO}$ for all the absorption lines identified prior to the `am` analysis. We subtracted the best-fitting linear continuum as described in Section 3.2. While the area of the best-fitting Gaussian function could be adopted as the $W_{\rm CO}$ value, we preferred to extract absorption line strengths by integrating over the channels clearly containing CO absorption to avoid any mismatch between the model and real spectrum.

During this process, flux densities at each frequency were scaled by the channel width in Hz before being summed over the entire frequency range. The integrated value still remains negative as the absorption feature corresponds to a dip that is negative in flux density when the continuum is subtracted. By convention, however, $W_{\rm CO}$ is positive, so we flipped the sign of $W_{\rm CO}$ after integration. The conventional unit of $W_{\rm CO}$ is K km s^{-1}, thus we need to convert flux density in Jy units to K and frequency from Hz to km s^{-1}. The Jy-to-K conversion is intrinsic to each observation. We picked a fixed position on the spectrum and read the flux density in both Jy and K. The ratio between the flux densities in Jy and the flux densities in K will give the Jy-to-K conversion. To convert Hz to km s^{-1}, we use the formula

$$v_{channel} = c * (1 - \frac{\nu_{observed}}{\nu_{rest}}) \tag{3.7}$$

with c in km s^{-1} unit to convert frequency in Hz into velocity in km s^{-1}.

After determining these $W_{\rm CO}$ values, the column density of hydrogen gas can be calculated in each case as:

$$N_{\rm H_2} = X_{\rm CO} W_{\rm CO} \tag{3.8}$$

where $X_{\rm CO}$ [in cm^{-2} (K km s^{-1})$^{-1}$ units] is the conversion factor to convert CO absorption line strength $W_{\rm CO}$ [in K km s^{-1}] into an H_2 column density. The correct conversion factor is not known for the center of M87, or for the centers of more than a handful of galaxies, so we adopted an $X_{\rm CO(0-1)}$ of 1.426×10^{20} cm^{-2} (K km s^{-1})$^{-1}$ (Eckart et al. 1990) that is typical of gas in active galactic nuclei, although we note that other literature sources typically assume values in the range of $(X_{\rm CO}/10^{20}) \approx 2.0 \pm 0.6$ for quiescent targets.

We propagated the error in $W_{\rm CO}$ by multiplying the standard deviation in flux density in the linear part of the continuum with the channel width and the square root of the total number of channels that make up the feature. The same unit conversion is applied to this uncertainty to convert from Jy Hz to K km s^{-1}. The uncertainty in $N_{\rm H_2}$ is propagated by multiplying the error in $W_{\rm CO}$ with the conversion factor for each transition.

The above CO-to-H_2 conversion factor only applies to the CO(1−0) absorption transition. To convert this to $X_{\rm CO(1-2)}$ and $X_{\rm CO(2-3)}$, we adopted typical Milky Way CO line luminosity ratios (e.g., see Boizelle et al. 2017), where the estimated ratios between absorption line depths are CO(1−2)/CO(0−1)≈0.6 and CO(2−3)/CO(0−1)≈0.24. to convert between different transitions. Other galaxy nuclei show larger ratios of high-to-low J absorption line depths (e.g., Carilli & Walter 2013), but currently there is not a reliable proxy that is sufficiently similar to the M87 nucleus conditions, so we retain the Milky Way line ratios. In addition to the 30% uncertainty in the ground-level $X_{\rm CO}$ factor, these line ratios are rarely known for an individual galaxy (or region of a galaxy) and remain uncertain at the factor of ∼2 level (Spilker et al. 2014). In addition, the absolute flux scaling of ALMA data sets is known to have an uncertainty of about 10% at the frequencies covered by this project. All together, the total error budget means that each $N_{\rm H_2}$ value is best viewed as an estimate.

Results of the measured $W_{\rm CO}$ are presented and discussed in Section 4.3.

3.4 Emission Lines

Aside from the range of velocities determined for individual cloud components, absorption-line studies do not reveal much about the gas kinematics in locations *around* the nucleus. For that we turn to emission line kinematics using the same CO tracer.

A bright nuclear continuum source often obscures faint CO emission in the circumnuclear region. Even when the emission is spatially distinct from the nucleus, deconvolution errors introduce large sidelobe features about the bright continuum

source. With high angular resolution and sensitivity, ALMA has shown the best view of faint CO emission to date and, in some cases, enabled gas-dynamical modeling that tightly constrain the BH mass (e.g., Boizelle et al. 2019). We studied the gas dynamics of M87 based on the diffuse emission features we identified in programs 2015.1.00030.S and 2016.1.00021.S. We can relate the peak emission frequency $\nu_{\rm obs}$, rest-frame frequency ν_0, and Doppler-shifted line-of-sight (LOS) velocity $v_{\rm LOS}$, with

$$\nu_{\rm obs} = \frac{\nu_0}{1+z}(1 - v_{\rm LOS}/c) \ . \tag{3.9}$$

A typical assumption is that the CO emission traces a thin disk of gas at the center of M87. The disk has an inclination angle of i (with $i = 0°$ is a face-on orientation and $i = 90°$ is edge-on). If the disk is assumed to be in circular rotation around the central BH, the circular velocity v_c of CO-emitting clouds can be calculated as

$$v_c = \frac{v_{\rm LOS}}{\sin(i)} \ . \tag{3.10}$$

Combining Newton's Universal Gravitational Law and centripetal acceleration, the circular velocity very near the BH is related to $M_{\rm BH}$ by

$$v_c^2 = \frac{GM_{\rm BH}}{r} \tag{3.11}$$

where r is the distance of a gas cloud to the BH. Assuming the gas is in circular motion around its central BH, we can infer the distance of the CO gas from the peak frequency of the emission feature we identified. When estimating the characteristic radius r (in pc) of the CO emission, we adopt a redshift value of $z = 0.00428$, an $i = 45$ degrees based on ionized atomic gas kinematics (Walsh et al. 2013), $G = 0.004302$ pc $M_\odot^{-1}$ (km s^{-1})^2, and $M_{\rm BH} = 6.5 \times 10^9$ $M_\odot$ (Event Horizon Telescope Collaboration et al. 2019). It is by no means certain that the ionized atomic and molecular gas share the same kinematic properties, although in some cases they are closely correlated (e.g., Neumayer et al. 2007).

We estimated the error in velocity along line of sight, $\sigma_{v_{LOS}}$, by width of Gaussian fit to the emission $\times$ 1.00428 $\times$ c/ν_{peak}. The uncertainties in $v_{centripetal}$ is propagated by $\sigma_{v_{LOS}}$/sin(i) and the uncertainties in distance to nucleus, σ_d, is propagated as $\sqrt{(-(5.59 \times 10^7 \times v_{LOS}^{-3} \times \sigma_{v_{LOS}}))^2}$.

Instead of extracting a single point profile, we used a spatial aperture centered on the central pixel of the image and integrated over the aperture to get the spectrum as a function of frequency. In order to minimize the noise and capture as much emission feature as possible, we varied the aperture size in a curve-of-growth analysis to include as much real feature distributed over the primary beam as possible. The radius of the aperture varies from the size of synthesized beam to slightly larger radii until all the high S/N pixels appear to be covered within the aperture. $I_{\rm CO}$ is calculated by numerical integration as before. We divided the integrated number by the beam size of each observation to convert Jy/beam to Jy. Error budgets for each radius were determined by analyzing a neighboring, relatively linear segment of the spectrum. We divide $I_{\rm CO}$ by the error budgets to estimate the S/N ratio and determine the optimal spatial aperture.

The I_{CO} results are presented in Section 4.4 with comparison to previous studies using similar methods. The H_2 mass is estimated by computing $M_{\mathrm{H}_2} = \alpha_{\rm CO} L'_{\rm CO}$ where $\alpha_{\rm CO}$ is identical to $X_{\rm CO}$ in different units and

$$L'_{\rm CO} = 3.25 \times 10^7 \; I_{\rm CO} \frac{D^2}{(1+z)\nu_{\rm rest}^2} \; \mathrm{K\,pc^2\,km/s}\,, \tag{3.12}$$

for the galaxy distance D (in Mpc) and the rest frequency $\nu_{\rm rest}$ (in GHz) (Carilli & Walter 2013). Adopting a value of $\alpha_{\rm CO} = 3.1\ M_\odot\ \mathrm{pc}^{-2}\ (\mathrm{km/s})^{-1}$ that is typical for the central kpc of bulge-dominated galaxies (Sandstrom et al. 2013), the I_{CO} values in Tables 4.3, 4.4, and 4.5 suggest less than $6 \times 10^6\ M_\odot$ of H_2 within the central few parsecs of the M87 nucleus. Since these emission-line measurements are not finalized, the resulting M_{H_2} is taken as an estimate only.

CHAPTER 4: Results and Discussion

This chapter presents the results of ratio test from Section 3.1, model fitting analysis from Section 3.2, W_{CO} measurements from Section 3.3, and I_{CO} measurements from Section 3.4. We also present the derived Hydrogen column densities and gas kinematics. With comparisons made to previous studies of other ETGs, we found our results, although with some uncertainties present in our assumption, on reasonable scales.

4.1 Frequency Ratio Test Results

The feature in program 2013.1.00073.S (Aug 16) centered at 229.59 GHz (Figure 2.5) is the deepest absorption line with the largest S/N ratio of ∼20. We anchor our frequency ratio tests on this feature as it is easily distinguishable from continuum noise. Note that while we discuss in Section 2.4 the fact that this sharp line is almost assuredly primarily atmospheric in nature, here and in Section 4.2.2 we use the original feature before removing the flags as these comprise a standard approach in studying gas in front of bright continuum sources.

After imaging the MS into data cubes at the native channel spacing, we also identified absorption features at 114.81 GHz in program 2012.1.00661.S (7 Mar 2014) and at 344.412 GHz in program 2012.1.00661.S (28 Jan 2014). When comparing the frequencies of CO transition lines at z=0.00428 from Spalatogue, these lines correspond to CO(1−0) and CO(3−2) absorption lines at this redshift, respectively.

Using the formalism described in Section 3.1, we anticipated the ratios of absorption line centroids to follow the ratios of rest frequencies: $\nu_{1-2}/\nu_{0-1} = 2.000$, $\nu_{2-3}/\nu_{1-2} = 1.500$. Based on the features described above, the observed ratios of these redshifted frequencies are $\nu_{1-2}/\nu_{0-1} = 1.999$ and $\nu_{2-3}/\nu_{1-2} = 1.500$. Since the ratios of observed frequencies agree well with that of rest frequencies, we conclude that these transitions are at appropriate frequencies based on our preliminary calculation.

Although the other CO(2−1) absorption lines were not tested, the frequencies of their centroids are all within ±1% of the expected redshifted frequency of the CO(2−1) transition. Thus the results of ratio tests on them would not be much different from the deep absorption line in program 2013.1.00073.S. We therefore consider these absorption features to be real absorption lines at the redshift of – and arising from within – M87.

4.2 Model Fitting Results

The best-fit parameters for our model are presented in Table 4.1, including the slope in Jy/GHz (Column 1) and y-intercept in Jy of the linear function fitting the continuum (Column 2), the number of Gaussian functions we implemented in our model if there were any used (Column 3), the peak amplitude(s) in Jy (Column 4), the centroid(s) in GHz (Column 5), the width(s) in MHz of the Gaussian function(s) (Column 7), and reduced chi-squared $\tilde{\chi}^2$ (Column 8). The continuum slopes around the CO(2−1) and CO(3−2) transitions are small enough and can be considered to be zero. This is consistent with our spectra presented in Section 2.3, where most spectra are almost flat and do not have a significant slope in their continuum. This also agrees with our `am` modeling results in Section 2.5, which showed that most transmittance profiles do not have a significant gradient. Observations like programs 2012.1.00661.S (Mar 7) and 2016.1.00021.S have larger and negative slopes. These observations cover the range of 114−115.5 GHz. As we expect from our `am` results in Figure 2.10 (top left), there is a significant drop in transmittance within that frequency range. Thus the overall decrease in flux densities in these two observations covering the CO(1−0) transition is consistent with our `am` predictions and likely represents a broad decrease between ALMA Bands that is caused by water vapor and has not been fully corrected. The $\tilde{\chi}^2$ varies in a range of 0.538 to 2787. The observations with strong detections, a line depth of more than 0.01 Jy, have better $\tilde{\chi}^2$ closer to 1. Thus a better model fitting result require the signal be strong enough to distinguish it from the systematic noise.

Linear Parameters		# of	Gaussian Parameters			$\tilde{\chi}^2$
slope	y-intercept	Gaussian	Peak (Jy)	Centroid (GHz)	Width (MHz)	
2012.1.00661.S Mar 7 CO(0−1) 113.85−115.72 GHz						
-0.02163	4.551	1	-0.0111	114.812	25.09	0.744
-0.03718	-2.208	2	-0.0048	114.803	4.10	0.527
			-0.0048	114.824	8.34	
2012.1.00661.S Jan 28 CO(2−3) 343.41−345.28 GHz						
-0.00740	3.5609	1	-0.0036	344.412	7.49	0.538
2013.1.00073.S Jun 14 CO(1−2) 228.63−230.50 GHz						
-0.00217	1.499	0				
2013.1.00073.S Aug 16 CO(1−2) 228.63−230.50 GHz						
0.00117	1.43	1	-0.0787	229.597	3.90	1.097
0.00117	1.43	2	-0.0450	229.596	1.78	0.9831
			-0.0456	229.597	5.49	
0.00117	1.43	3	-0.0470	229.596	1.80	
			-0.0437	229.597	5.60	
			-0.00442	229.600	0.42	0.982
new 2013.1.00073.S Aug 16 CO(1−2) 228.63−230.50 GHz						
-0.00217	1.499	0				
2016.1.00021.S CO(0−1) 113.85−115.72 GHz						
-0.00699	2.5198	1	-0.0039	114.807	2.71	1.261
2016.1.01154.V Apr 5 CO(1−2) 228.17−230.04 GHz						
-0.00292	1.7959	1	-0.0163	229.582	31.27	0.984
2016.1.01154.V Apr 6 CO(1−2) 228.17−230.04 GHz						
0.00319	0.3685	1	-0.0077	229.586	23.97	2.787
2017.1.00841.V Apr 20 CO(1−2) 228.17−230.04 GHz						
-0.00062	0.8506	1	-0.0051	229.593	23.66	1.654
2017.1.00841.V Apr 21 CO(1−2) 228.17−230.04 GHz						
-0.00317	1.4373	1	-0.0051	229.594	24.00	1.384

TABLE 4.1: CO absorption line parameters.

We compared the centroids of each respective CO transition and find most of them to be consistent to 1% within the uncertainties, even if we consider the multi-Gaussian model fit to program 2012.1.00661.S (Mar 7). This also agrees with our predictions from line ratio tests, adding additional support that these

features are real absorption from gas near the center of M87.

4.2.1 Decomposing the 2013.1.00073.S Aug 16 absorption line into multi-Gaussian absorption components

Figure 4.1 presents the results when decomposing the deep absorption feature in program 2013.1.00073.S using different Gaussian fit models. The 1-Gaussian model under-fits the feature, with a reduced chi-squared of 1.097. The 2-Gaussian model and the 3-Gaussian model have a reduced chi-squared of 0.9831 and 0.9818 respectively. While there is some improvement in reduced chi-squared values going from 1-Gaussian to 2-Gaussian and finally 3-Gaussian models, the 2-Gaussian model returns a χ^2_{dof} that is very close to that of the 3-Gaussian one. Certainly, the addition of three more free parameters is not reflected in a significantly improved goodness of fit. The components of 2-Gaussian and 3-Gaussian models are not very different visually, with the third Gaussian having very low amplitude. Thus we conclude that both qualitatively from Figure 4.1 and quantitatively from reduced chi-squared values that the 2-Gaussian model is the most reasonable fit to the data.

If the two Gaussian functions were to represent real absorption lines against the M87 continuum source, we do see that they have slightly different centroids, The more narrow one is centered on 229.596 GHz and the more broad one is centered on 229.597 GHz. With these two frequencies we can calculate the radial velocities of the sources corresponding to these two absorption lines with

$$v_{\text{source}} = c\left(1 - \frac{\nu_{\text{rest}}}{\nu_{\text{obs}}}\right) \tag{4.1}$$

where ν_{rest} = 230.538 GHz. A 229.596 GHz absorption line corresponds to a radial velocity of 1225.83 km s^{-1} and the one at 229.597 GHz corresponds to 1224.53 km s^{-1}. Based on this approach, the two sources would have a difference in radial motion of roughly just 1.3 km s^{-1}. If this feature corresponded to real gas clouds, then the v_{radial} are only slightly smaller than the recessional velocity of M87, which is 1284 km s^{-1}. Note that the velocity difference in the centroids

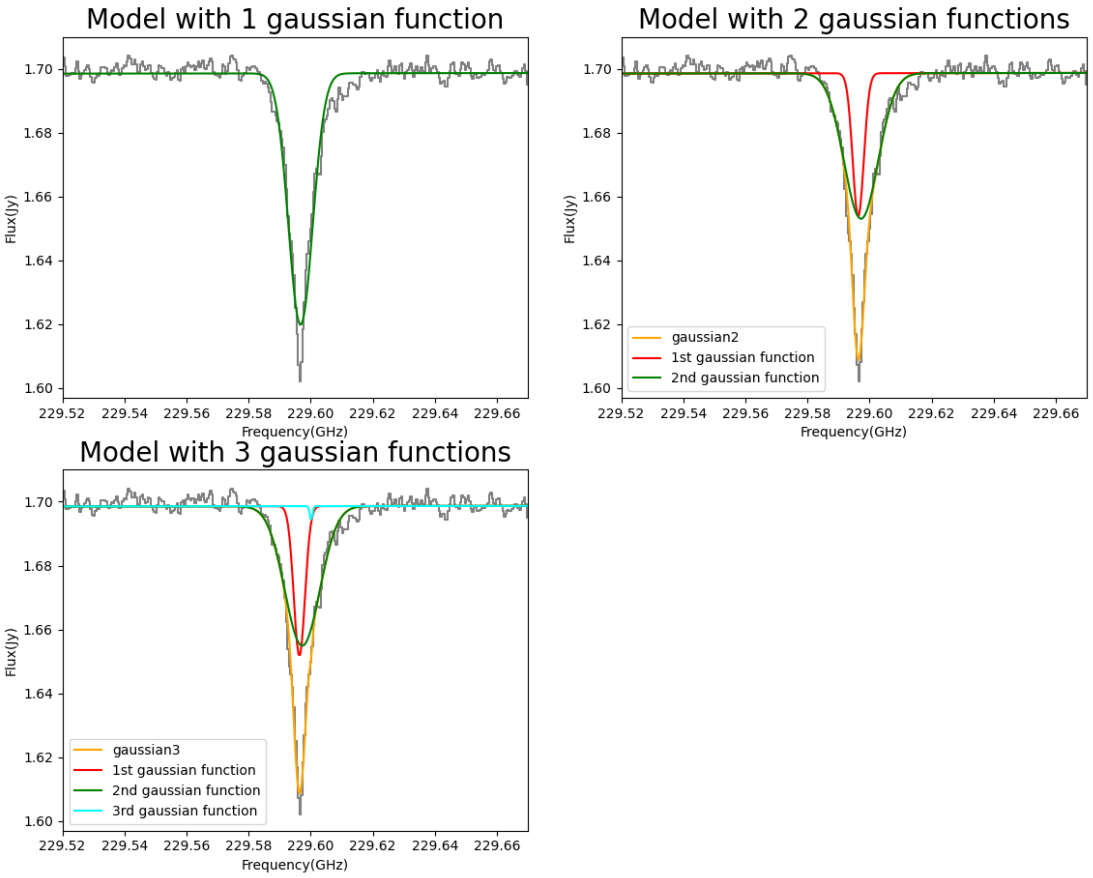

FIGURE 4.1: Gaussian fitting for the deep absorption line in program 2013.1.00073, assuming either multiple clouds along the line of sight on that the absorption may partially due to the absorption in atmospheric molecules. Visually 2-Gaussian model has already captured the asymmetric shape near 229.61 GHz. The reduced chi-squared values for these models are: 1.097 for 1-Gaussian, 0.983 for 2-Gaussian, and 0.982 for 3-Gaussian. Our best-fit model is the 2-Gaussian model.

of two components is typically below the $\sim$8 km s^{-1} velocity dispersion of gas particles within a single cloud of perhaps 10 pc radius (Utomo et al. 2015).

If we were to assume that this deep absorption feature were entirely real, this decomposition would explore whether the gas was separated into the multiple layers of clouds along line of sight. In this case, we do not find strong evidence for kinematically distinct clouds, although the observed asymmetry is interesting. Two possible explanations exist – either the gas velocity distribution is not perfectly represented by a symmetrical Gaussian, or the real CO(1−2) absorption line is slightly offset from the atmospheric O_3 transition.

We have calculated the best-fit parameters with `least_squares`, but the uncertainties are not determined. `least_squares` does not calculate the uncertainties, thus future analyses with Monte Carlo methods can be used to determine the uncertainties.

4.2.2 Decomposing the feature in 2013.1.00073 Aug 16 into atmospheric absorption and real absorption components from M87

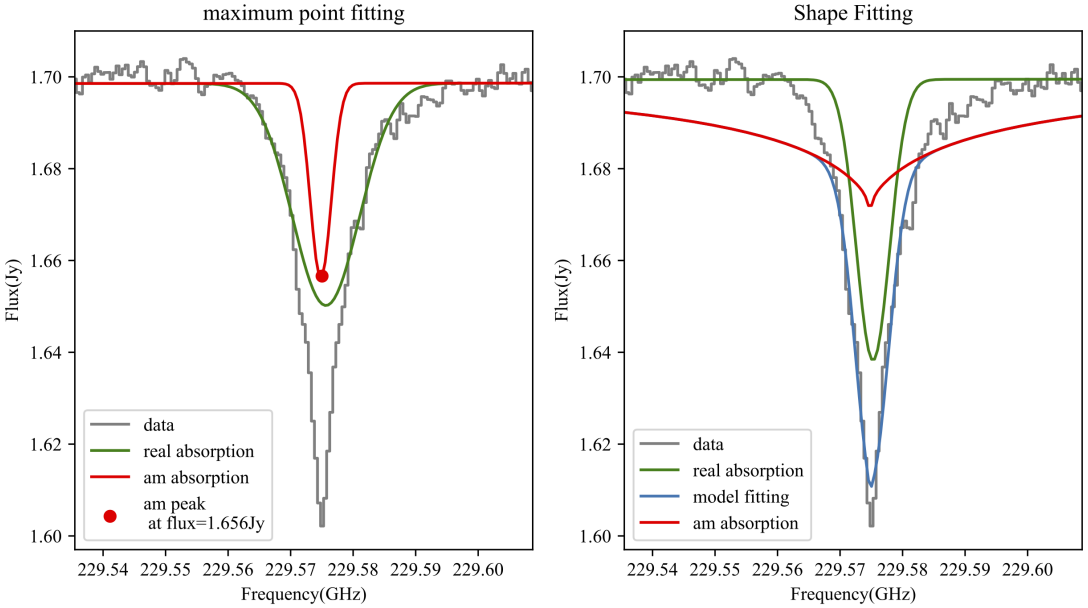

FIGURE 4.2: Gaussian fitting for the deep absorption line in program 2013.1.00073, assuming the absorption is partially due to absorption by atmospheric molecules. The fitting on the left fixed the height of the atmospheric ozone transition and allowed the width of the Gaussian function to vary. The fitting on the right fixed the shape of the ozone transition and left its height to vary. In both fitting, the parameters of the Gaussian functions were left free to best capture the entire observed feature in addition to the atmospheric ozone transition.

Figure 4.2 (left) shows the result of our first model. The feature is decomposed into the real absorption in green and the atmospheric absorption in the atmosphere. The modeled real absorption is centered at $\sim$ 229.578 GHz. It slightly deviates from the centroid frequency of the main feature at 229.575 GHz.

Figure 4.2 (right) shows the fitting of the second model. This model fixed the shape of the ozone absorption line but allowed its strength to vary. We do not know the correct column density of ozone in the atmosphere above ALMA as there is no model describing the atmosphere along the line of sight for us to use. We adopted the shape only but not the strength of the line. The calibrator J1229+0203 does not have any flags in 229.559–229.595 GHz. As a result, only within the range of 229.559-229.595 GHz would we expect the atmospheric ozone feature to appear. The absorption from atmospheric ozone builds up the base of the absorption feature from 229.565 GHz to 229.59 GHz. This range is slightly smaller than the unflagged region from calibrator J1229+0203. The rest of the observed feature in the spectrum is considered absorption from M87 as shown in the green Gaussian function in Figure 4.2 (right).

Thus we are able to provide two different ways of examining this feature and decomposing it into the uncleaned atmospheric absorption and the real feature. We think that the model with a fixed Gaussian shape (Figure 4.2 (left)) would better describe the two features than the model with varying width (Figure 4.2 (left)), because the former captures more of the characteristic of atmospheric ozone absorption. There are some limits to these two methods. We might need a more accurate atmospheric model describing the atmosphere above ALMA to gain a better result even if the atmospheric feature has not been cleaned. After the first round of cleaning performed by ALMA staff, we are unsure how many atmospheric features still remain in the spectrum. With these uncertainties, we cannot determine a fully accurate model that describes the two features. However, these methods still provide a way to look at these features that may be a mixture of absorption from the target and atmospheric transitions, if a more accurate model is provided.

4.3 W_{CO} Results and Analysis

We present our $W_{\rm CO}$ and $N_{\rm H_2}$ values with their uncertainties in Table 4.2, listing the observation dates (Column 1), the type of transition (Column 2), W_{CO} in K km s^{-1} with uncertainties (Column 3), and molecular hydrogen column densities in

cm^{-2} with uncertainties. Most $W_{\rm CO}$ are within $0.7-10.85$ K km s^{-1} and most $N_{\rm H_2}$ are within $(0.168-2.579)\times10^{21}$ cm^{-2} (not accounting for systematic error terms, e.g., due to the uncertain $X_{\rm CO}$ factor). The two observations with $W_{\rm CO}$ values larger than 90 K km s^{-1} and $N_{\rm H_2}$ larger than 20×10^{21} cm^{-2} are 2016.1.00021 (Aug 15) and 2013.1.00073 (Aug 16, old). As discussed in Section 2.4, we have verified that the feature in program 2013.1.00073 (Aug 16, old) is spurious and the result of channels of the bandpass calibrator being improperly flagged during manual calibration. This explains why the $W_{\rm CO}$ and $N_{\rm H_2}$ values from this observation are higher than the others and we exclude these results in our analysis.

Understanding the discrepant results from program 2016.1.00021 (Aug 15) is more challenging. Integrating this data returns a $W_{\rm CO}$ of 149.21 ± 25.371 K km s^{-1} and an $N_{\rm H_2}$ of 21.28×10^{21} cm^{-2}, roughly an order of magnitude higher than the other $N_{\rm H_2}$ values. One possible explanation could be that cloud positions (or continuum emission distribution from the jet region) change over ∼year timescales, resulting in observations probing a different column density of gas. Another possible explanation could be that the higher values may be tied to the higher angular resolution. The maximum baselines of the ALMA observations that show CO absorption features are typically less than 1.5 km while program 2016.1.00021 (Aug 15) was obtained using a maximum baseline of 3.64 km. Following the equation that the spatial resolution in arcsec can be approximated as $76/\max_{\rm baseline}$[km]/frequency[GHz][1], program 2016.1.00021 (Aug 15) has an angular resolution at least twice as sharp as the other observations and has both the largest $W_{\rm CO}$ and $N_{\rm H_2}$ values of all observations. More study is needed to explore the possible effect of synthesized beam size on the recovered $W_{\rm CO}$ value.

Excluding programs 2016.1.00021 (Aug 15) and 2013.1.00073 [Aug 16(old)], CO(1−0) and CO(3−2) transitions only have one $W_{\rm CO}$ and $N_{\rm H_2}$ values each. The conversions of $W_{\rm CO(1-2)}$ to $W_{\rm CO(2-3)}$ and of $W_{\rm CO(1-2)}$ to $W_{\rm CO(0-1)}$ are rough estimates and, together with the $X_{\rm CO}$ factor, introduce large uncertainties into the corresponding $N_{\rm H_2}$. Thus we place greater emphasis on comparisons between the other 6 estimates derived from the same CO(2−1) transition. These more homogeneous set of observations have a well-distributed set of $N_{\rm H_2}$ between $(0.168-2.579)\times10^{21}$ cm^{-2} with an average of 1.004×10^{21} cm^{-2} and a median of 0.6465×10^{21} cm^{-2}.

[1] https://almascience.eso.org/about-alma/alma-basics

N_{H_2} also varies within the same program, e.g., if we compare within the three programs, 2013.1.00073, 2016.1.01154, and 2017.1.00841. Observations in the same program still have different array configurations and different synthesized beam size, as shown in Table 1 (ALMA Imaging, column 4 and column 5). With different resolutions and different spatial coverages, we expect N_{H_2} to vary somewhat. Future work will need to explore the reasons for the spread in column densities.

Previous studies used the same technique to derive column densities of molecular hydrogen in different galaxies. ALMA CO(1−2) absorption line measurements of similar ETGs NGC 4374 and IC 4296 have an estimated W_{CO} of (19.4 ± 2.5) and (44.3 ± 1.4) K km s^{-1} and slightly higher N_{H_2} of $(4.7 \pm 0.6) \times 10^{21}$ and $(11 \pm 3) \times 10^{21}$ cm^{-2} along the line of sight, respectively (Boizelle et al. 2017). In another ALMA study of Hydra-A, a brightest cluster galaxy with a thick, nearly edge-on dusty disk, a similar technique required more Gaussian functions to fit the absorption line spectrum (Rose et al. 2020). From CO(2−1) absorption lines, the gas has a CO column density of N_{CO} $\sim 3.99 \times 10^{15}$ cm^{-2} along line of sight. Using an approximate CO/H_2 abundance ratio of $\sim 10^{-4}$ (France et al. 2014), we convert the N_{CO} of Hydra-A to N_{H_2} and get an estimate for N_{H_2} of 2.67×10^{19} cm^{-2}. Our N_{H_2} results lie between the column densities of these two former analyses, and we consider (most of) the N_{H_2} measured against the M87 nucleus to be reasonable estimates for column densities in this type of ETG.

We also estimate the V-band extinction A_V with the linear relationship between optical extinction A_V and column density of *atomic* hydrogen N_H from Güver & Özel (2009)

$$N_H\,[\mathrm{cm}^{-2}] = (2.21 \pm 0.09) \times 10^{21} A_V \ . \tag{4.2}$$

Using a conversion of N_{H_2}/N_H=2 and the average $N_{H_2} \sim 1.004 \times 10^{21}$ cm^{-2}, the estimated A_V is 0.91 mag. With an A_V that is ~ 1, we expect that there is significant dust present in the disk of M87 that is causing this extinction, but the EHT images reveal little dust features near the nucleus. This could be either because the dust is efficiently destroyed in the nucleus of M87, leaving only the atomic and molecular gas in the disk; or we are seeing absorption through a section of optically thick cloud in the circumnuclear region, where one of many optically thick clouds happen to pass by the line of sight. Uncertainties and assumptions

Observation	**Transition**	W_{CO} (K km s^{-1})	$N_{\mathrm{H_2}}$ (10^{21} cm^{-2})
2012.1.00661 Mar 7	CO(0-1)	8.30 ± 0.559	1.183± 0.079
2016.1.00021 Aug 15	CO(0-1)	149.21 ± 25.371	21.28±3.62
2013.1.00073 Aug 16(old)	CO(1-2)	99.22 ± 0.889	23.58±0.127
2013.1.00073 Aug 16(new)	CO(1-2)	10.85 ± 0.891	2.579±0.127
2013.1.00073 Jun 14	CO(1-2)	7.45 ± 6.004	1.771±0.856
2016.1.01154 Apr 5	CO(1-2)	3.39 ± 0.214	0.806±0.031
2016.1.01154 Apr 6	CO(1-2)	0.70 ± 0.049	0.168±0.007
2017.1.00841 Apr 20	CO(1-2)	2.05 ± 0.135	0.487±0.019
2017.1.00841 Apr 21	CO(1-2)	2.35 ± 0.333	0.583±0.048
2012.1.00061 Jan 28	CO(2-3)	0.89 ± 0.240	0.211±0.034

TABLE 4.2: The integrated CO absorption line strength and hydrogen column densities.

in the conversion we made can be another reason that causes the extinction to be higher than what we would expect.

4.4 Emission-line Spectra and I_{CO} analysis

We present the continuum-subtracted spectra on peak-intensity pixel for programs 2012.1.00661.S (Jan 28), 2015.1.00030.S, and 2016.1.00021.S in Figure 4.3, Figure 4.4, and Figure 4.5. The highlighted regions in programs 2015.1.00030.S and 2016.1.00021.S are the regions with a feature we identified as emission and thus are the selected channels for I_{CO} integration. After running the `uvcontsub` task on the program 2016.1.00021.S MS, the resulting spectrum is fairly continuous; for program 2015.1.00030.S, however, the continuum-subtracted spectrum has a minor jump near 114.0 GHz where the two spectral windows overlaps. Ongoing `uvcontsub` trials have not found the right range of continuum channels to remove this jump and an apparent positive gradient at larger frequencies. Some of the problems may be due to the spectral windows in program 2015.1.00030.S having a smaller (0.31 GHz) overlap compared to the overlap (0.64 GHz) for program 2016.1.00021.S. In both cases, the spectral coverage is not sufficient at the highest frequencies to confidently constrain the continuum contributions on that side of the emission.

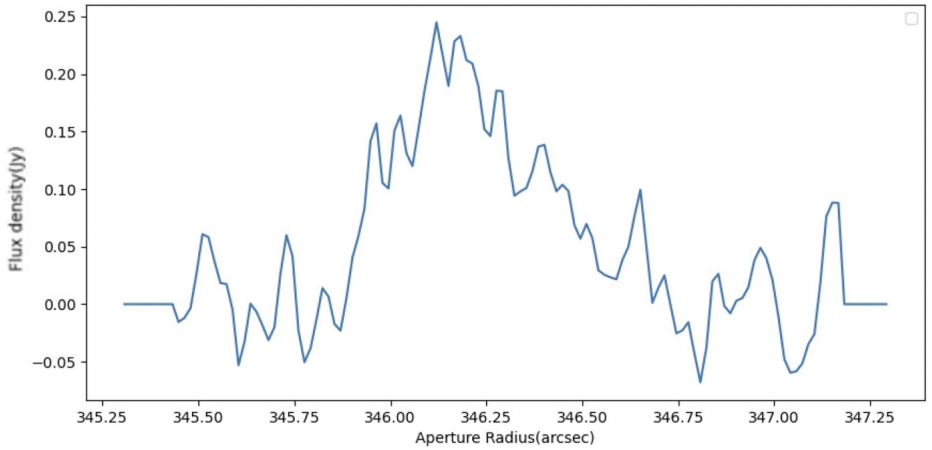

FIGURE 4.3: 2012.1.00661 Jan 28 continuum-subtracted spectrum at peak-intensity pixel. The emission feature centered at $\sim$ 346.2 GHz extends from 345.75 GHz to 346.75 GHz. The continuum is zeroed and the emission feature is more prominent after the continuum subtraction, compared to Figure 2.2 (bottom).

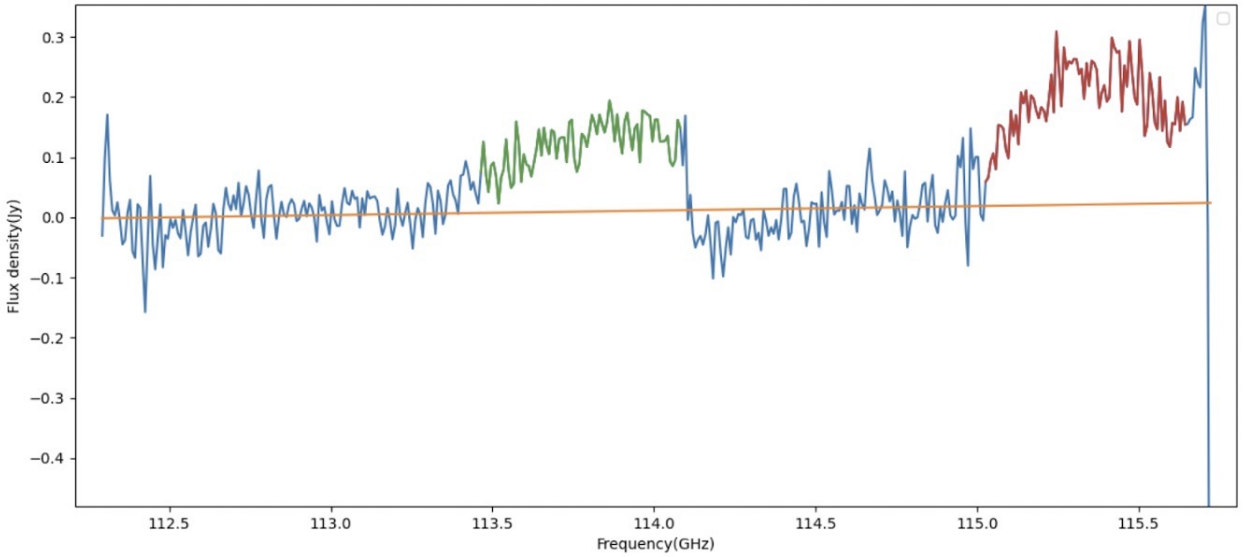

FIGURE 4.4: 2015.1.00030.S continuum-subtracted spectrum at peak-intensity pixel. Two broad emission features, in green and red, extend from 113.45 GHz to 114.0 GHz, and from 115.1 GHz to 115.5 GHz, respectively. The yellow horizontal line shows a linear fitting of the channels in blue. The two spectral windows cover 112.28–114.16 GHz and 113.85–115.72 GHz respectively, and the region from 113.85–114.16 GHz is where the two spectral windows overlap with each other. The discontinuity near 114.0 GHz is caused by combining two spectral windows together after they are continuum-subtracted. Bad channels are present at 115.7 GHz with uncertainties in the flux densities. We exclude them from the feature when calculating I_{CO}.

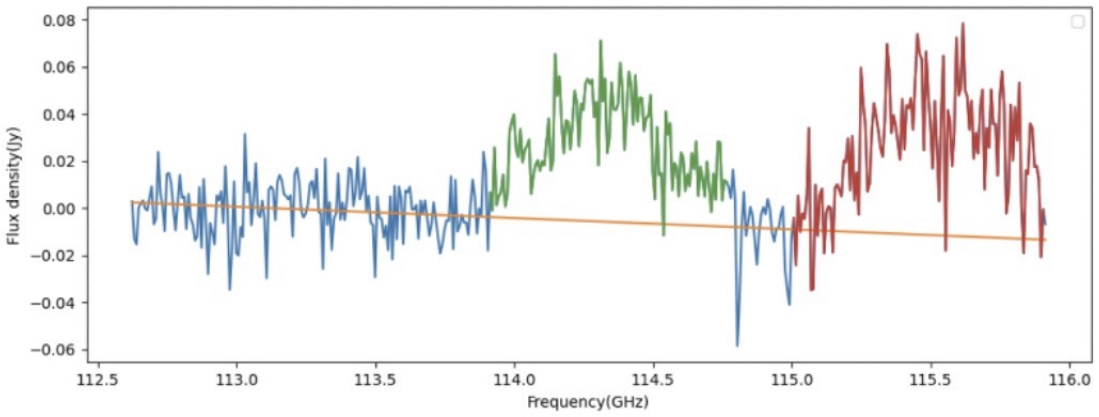

FIGURE 4.5: 2016.1.00021 continuum-subtracted spectrum at peak-intensity pixel. Two broad emission features, centered on 114.4 GHz and 115.5 GHz, are marked in green and red respectively. The green feature extends from 114.0 GHz to 114.7 GHz. The red feature extends from 115.0 GHz and to the end of this spectral window. The channels marked in blue are the channels used for linear fitting and the linear model is the horizontal line marked in yellow. This spectrum, combined from three spectral windows, is more continuous and smooth compared to the continuum-subtracted spectrum of 2015.1.00030.S (Figure 4.4) because there is greater frequency overlap in the spectral windows.

The continua are flattened and zeroed with only minor slopes, as we would expect after running the `uvcontsub` task. Systematic noise is still present in all three spectra, but the emission features are more prominent compared to the spectra presented in Section 2.3. Program 2012.1.00661.S (Jan 28) has a single emission feature centered on 346.2 GHz. It does not have the other symmetric feature on the left hand side of 344.32 GHz, the expected $\nu_{\rm obs}$ of the CO(3−2) transition. We could not detect it because the spectral setup did not cover the low-frequency region of interest (∼341.9−342.9 GHz). On either side of $\nu_{\rm obs} = 114.78$ GHz, we find what appears to be symmetric CO(1−0) emission features in both programs 2015.1.00030.S and 2016.1.00021.S. The emission features in program 2015.1.00030.S have peak flux densities of 0.2 Jy and 0.3 Jy, stronger than the emission features in program 2016.1.00021.S, where the peak values only reach ∼0.08 Jy. Again, we reiterate that we are not confident that the spectral coverage at higher frequencies are sufficient to remove the continuum emission. The CO emission features might be cut off if they extend beyond the frequency coverage.

The integrated $I_{\rm CO}$ with varying aperture sizes, its uncertainties, and S/N are presented in Table 4.5, Table 4.4, and Table 4.3 for each emission feature in each

		114.34 GHz			115.5 GHz		
r (pixel)	**r (arcsec)**	I_{CO} **(Jy km s^{-1})**	$\sigma_{I_{CO}}$	**S/N**	I_{CO} **(Jy km s^{-1})**	$\sigma_{I_{CO}}$	**S/N**
4	0.12	1.2570	0.0491	25.59	1.2100	0.0504	23.99
5	0.15	1.5911	0.0630	25.27	1.5528	0.0647	24.01
6	0.18	1.9048	0.0796	23.94	1.9308	0.0817	23.63
7	0.21	2.0360	0.0920	22.13	2.1695	0.0945	22.96
8	0.24	2.1522	0.1061	20.29	2.4644	0.1089	22.62
9	0.27	2.2334	0.1196	18.67	2.7554	0.1228	22.43
10	0.3	2.2978	0.1308	17.56	2.9859	0.1344	22.22
11	0.33	2.3796	0.1431	16.63	3.2040	0.1470	21.79
12	0.36	2.4279	0.1540	15.76	3.2864	0.1582	20.77
13	0.39	2.5208	0.1666	15.14	3.3999	0.1711	19.87
14	0.42	2.5785	0.1794	14.38	3.4439	0.1953	17.63
15	0.45	2.6393	0.1901	13.88	3.5000	0.1953	17.92
16	0.48	2.6728	0.2002	13.35	3.5661	0.2056	17.34
17	0.51	2.6817	0.2095	12.80	3.6161	0.2152	16.81

TABLE 4.3: 2016.1.00021.S I_{CO} from an aperture with varying radius r. Two emission features are centered at 114.34 GHz and 115.5 GHz (Figure 4.5). The noise is propagated with the linear continuum of a nearby background region from the source in the center.

observation. As we expect, I_{CO} increases as aperture size increases because more flux is included. Its rate of change is high for the first few pixels and decreases significantly thereafter. The first few apertures cover primarily the synthesized beam area, and the strong signal suggests that much of the CO emission is unresolved, at least when using observations with a beam size of $\sim 0.2''$ (roughly 15 pc physical resolution at the distance of M87). Going further beyond the synthesized beam and into the noise-dominated region, we find a decrease in both the rate of change in I_{CO} and in the total S/N ratio.

The S/N ratio is high at the first few pixels but drops even before I_{CO} starts increasing slower, because the sensitivity of the beam is higher closer to the center of the beam. Going further from the center thus includes pixels with lower sensitivity and thus relatively lower flux.

For the emission features centered on 114.34 GHz and 115.5 GHz in program 2016.1.00021.S, we found a combined $I_{CO(1-0)}$ values to be $2.68 + 3.61 = 6.29$ Jy km s^{-1}. For the emission features centered at 113.75 GHz and 115.3 GHz in program 2015.1.00030.S, the maximum $I_{CO(1-0)}$ values we integrated are $9.03 +$

		113.75 GHz			115.3 GHz		
r (pixel)	**r (arcsec)**	$I_{\rm CO}$ **(Jy km s^{-1})**	$\sigma_{I_{\rm CO}}$	**S/N**	$I_{\rm CO}$ **(Jy km s^{-1})**	$\sigma_{I_{\rm CO}}$	**S/N**
4	0.04	2.946	0.0770	38.27	4.718	0.136	34.61
5	0.05	3.960	0.096	41.46	6.265	0.183	34.24
6	0.06	5.382	0.129	41.67	8.205	0.247	33.27
7	0.07	6.372	0.167	38.13	9.415	0.279	33.76
8	0.08	7.411	0.201	36.95	10.59	0.313	33.86
9	0.09	8.181	0.216	37.94	11.40	0.346	32.99
10	0.1	8.658	0.226	38.26	11.86	0.355	33.40
11	0.11	8.926	0.234	38.08	12.11	0.370	32.69
12	0.12	9.032	0.239	37.77	12.16	0.385	31.63
13	0.13	8.972	0.264	33.96	12.13	0.404	30.04
14	0.14	8.716	0.291	29.90	11.88	0.428	27.76
15	0.15	8.366	0.313	26.76	11.63	0.444	26.20

TABLE 4.4: 2015.1.00030 $I_{\rm CO}$ from an aperture with varying radius r. Two emission features are peaking at 113.75 GHz and 115.3 GHz (Figure 4.4). The noise is propagated with the linear continuum of a nearby background region from the source in the center.

r **(pixel)**	r **(arcsec)**	$I_{\rm CO}$ **(Jy km s^{-1})**	$\sigma_{I_{CO}}$	**S/N**
3	0.30	1.31	0.0574	22.797
4	0.40	2.11	0.0814	25.910
5	0.50	2.86	0.0902	31.726
6	0.60	3.75	0.1003	37.378
7	0.70	4.35	0.1098	39.645
8	0.80	4.91	0.1342	36.638
9	0.90	5.37	0.1649	32.592
10	1.00	5.66	0.1968	28.765
11	1.10	5.81	0.2227	26.065
12	1.20	5.80	0.2304	25.168
13	1.30	5.69	0.2359	25.029
14	1.40	5.42	0.2406	22.540

TABLE 4.5: 2012.1.00661 I_{CO} from an aperture with varying radius r of the diffuse emission peaking at 346 GHz (Figure 4.3). The noise is propagated with the linear continuum of a nearby background region from the source in the center.

Project Code	**estimated peak ν (GHz)**	**v_{LOS} (km s^{-1})**	**v_c (km s^{-1})**	**d (pc)**
2015.1.00030.S	113.789	2,647.99±53.9	3744.83±44.19	1.99±0.32
	115.328	-1,395.38±31.2	-1973.37±76.19	7.18±0.18
2016.1.00021.S	114.259	1,360.46 ±62.1	1923.98±87.86	7.55±0.69
	115.485	-1,842.08±39.5	-2605.10±55.81	4.12±0.32 height

TABLE 4.6: Estimated peak frequency of each emission feature and analysis revealing the dynamics of the galaxy.

12.16 = 21.09 Jy km s^{-1}. The single emission feature centered at 346.2 GHz in 2012.1.00661.S has a maximum $I_{CO(3-2)}$ of 5.81 Jy km s^{-1}. The $I_{CO(2-1)}$ of 2016.1.00021.S is ∼4 times smaller than $I_{CO(2-1)}$ of 2015.1.00030.S, which could be due to the differences in spatial resolution and different field of view, as we see their maximum baselines and beam sizes are different from Table 1 ALMA Imaging. The accuracy of the continuum-subtracted spectrum of 2015.1.00030.S is unknown due to insufficient channels overlapping between two spectral windows. Comparing our $I_{CO(1-0)}$ results to the $I_{CO(2-1)}$ of two AGNs NGC 4374 and IG 4296, (4.81±0.7) Jy km s^{-1} and (0.76±0.18) Jy km s^{-1} (Boizelle et al. 2017), we found them similar to each other, as these two AGNs are ETGs like M87 and thus we would expect them to be similar in CO brightness. We consider our results to be reasonable and a good estimate of CO(2−1) emission from M87.

Assuming the CO gas that produced the CO(1−0) emission is in a perfectly rotating disk, we derived the velocity of CO gas along line of sight v_{LOS}, its centripetal velocity around the galactic nucleus v_c, and its distance to the nucleus d, of the two observations with CO diffuse emission and present our results in Table 4.6. We found a range of centripetal velocities of (-2605−+3744) km s^{-1} and the distance of gas to be (1.99−7.18) pc away from the nucleus. The radii probed by the CO-emitting gas are much larger than those captured in EHT observations (∼ 900 AU, or Solar System scales), which might be due to the small field of view (50 μas, 0.00423pc) that EHT is covering. The centripetal velocities are much larger than the centripetal velocities of CO from CO(2−1) line studies of NGC 4374 and IC 4296 from Boizelle et al. (2017), ± 520 km s^{-1} and ± 480 km s^{-1}. The CO gas in M87 is closer to the nucleus than the gas in NGC 4374 and IC 4296, which is ∼ 20–50 pc away from the nucleus. Thus we would expect the CO gas in M87 to have a larger centripetal velocity.

We are not sure if enough channels are provided at $\sim$115.5$-$116.0 GHz of both continuum observations in programs 2016.1.00021.S and 2015.1.00030.S. Future ALMA projects with wider spectral coverage are suggested to have longer coverage to capture these broad diffuse CO(1$-$0) emission features starting from 113.5 GHz and extending just beyond 116.0 GHz. Longer overlap between spectral windows of 0.7 GHz will be needed to yield a more continuous spectrum after combining spectral windows together.

CHAPTER 5: Conclusion

We presented our CO line search in 11 archival ALMA programs targeting M87 in ALMA Bands 3, 6, and 7. We identified 1 CO(1−0) absorption line at 114.80 GHz, two other pairs of symmetrical broad emission features around 114.78 GHz, and 6 CO(2−1) absorption lines that slightly deviate from the expected 229.59 GHz. The deviation of the absorption line centroids from the expected CO transitions with $z = 0.00428$ suggests that the gas producing this CO transition line has a velocity gradient along line of sight. Assuming a disk that is in circular motion around the galactic nucleus, the CO gas might not be in perfect circular motion, and with a velocity offset of $\sim$50 km s^{-1} from the recessional velocity of M87.

We also carefully examined the spectra we imaged and found a few concerns in blindly using pre-processed, manually-calibrated observations. One of these concerns is how well the atmospheric transitions were corrected. We calculated the transmittance profile of the atmosphere above Mauna Kea, an observatory at the same elevation as ALMA site. We used this transmittance profile from `am` and compared it to the continuum spectra we imaged for each observation. A few ozone absorption remnants are identified, which means the atmospheric features were not completely removed during data calibration. This led us to re-think the composition of identified CO absorption lines especially for M87, because the CO absorption lines are at the same frequencies as certain atmospheric ozone transitions. Another concern is the manually flagged calibrator from 2013.1.00073.S Aug 16 observation. It has caused an abnormally strong absorption line in the same frequency range as where the bandpass calibrator data was manually flagged. When exploring faint molecular line surveys, we advise an exploration of the atmospheric transmittance profile to avoid contamination from atmospheric ozone.

We calculated a $W_{\mathrm{CO(1-2)}}$ of (0.70−10.85) K km s^{-1} based on the identified CO(2−1) absorption lines. We estimated $N_{\mathrm{H_2}}$ along line of sight in M87 to be $(0.168-2.579)\times10^{21}\mathrm{cm}^{-2}$. These results agree with previous studies of similar AGNs and predict a hydrogen-rich composition of M87. Our I_{CO} analysis of two pairs of CO(1−0) diffuse emission present results of 6.29 Jy km s^{-1} from 2016.1.00021.S and 21.09 Jy km s^{-1} from 2015.1.00030.S. Program 2015.1.00030.S

does not have a perfect continuum-subtracted spectrum, thus there are some uncertainties in its $I_{\rm CO}$. But the $I_{\rm CO}$ from Program 2016.1.00021.S is on the same order of magnitude as previous studies of AGNs. Based on the diffuse CO(1−0) emission features, we derived a centripetal velocities for the CO gas and found a range of -2605.09 km s^{-1} to 3744.83 km s^{-1}. The CO gas in the disk of M87 seems to be moving much faster than the CO gas in NGC 4374. The distance from the galactic nucleus to the CO gas producing these emission features ranges from 1.99 pc to 7.55 pc, which implies a larger disk than the EHT images of M87.

We have imaged and examined diffuse CO emission present in the spectra of M87 around its CO(1−0) emission lines at 114.78 GHz and have derived reasonable results revealing some information of the dynamical structure.

Based on these archival observations, we believe that ALMA is in a good position to place more confident constraints on the gas kinematics if more observations are available regarding CO(1−0) emission. We expect from our observation that a good spectral setup for ALMA imaging will need high angular resolution of 0.05" in order to resolve the CO emission on pc-scales. This is only available currently with ALMA, which is able to provide an angular resolution from 0.012" to 3.4" with its 12-m array. However, with such a small synthesized beam, only C-9/10 configuration can produce an image on a size smaller than 0.05". Data taken within C-9/10 configuration is difficult to use due to the challenges in calculating phase corrections of long baselines. One might need to balance the need for angular resolution with the feasibility of very high-resolution imaging.

With the spectra , we expect the diffuse emission to extend from 113.5 GHz to frequencies beyond 116.0 GHz. Thus future ALMA imaging of CO(1−0) emission will require wide spectral coverage from 113.5 GHz to possibly 116.5 GHz. Long, continuous spectral coverage of ∼3-4 GHz is required to cover these CO(1−0) emission features. A wider overlap in frequency of spectral windows of > 0.5 GHz would be helpful for combining the data together and forming a longer spectrum that completely covers emission features. Based on the emission-line spectra in the previous section, these observations would need to be sensitive to a scale of 5 mJy/beam per channel with a width of 1.13 MHz.

APPENDIX A: Appendix A

We list all the spectra that are not discussed in Section 2.3 here in this Appendix. We include the programs 2013.1.01022.S, 2015.1.01170.S., 2015.1.01352.S, 2017.1.00608.S, and 2017.1.00842.S. They do not have any major emission and absorption features that we are interested in. They follow the same color scheme as the spectra in Section 2.3. Refer to Table 1 (ALMA Imaging) for more information.

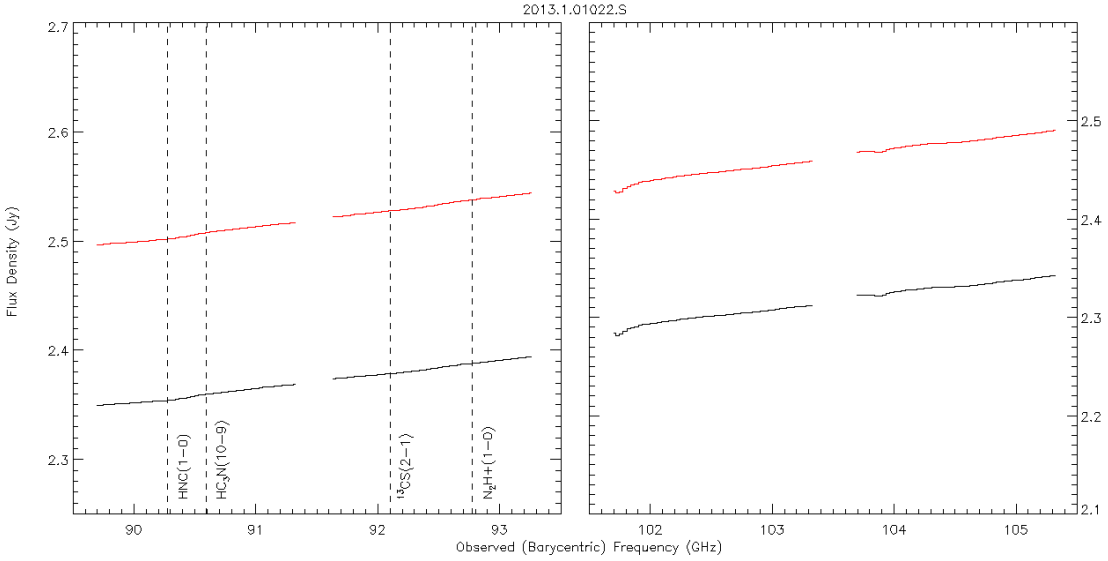

FIGURE A.1: 2013.1.01022.S continuum spectra.

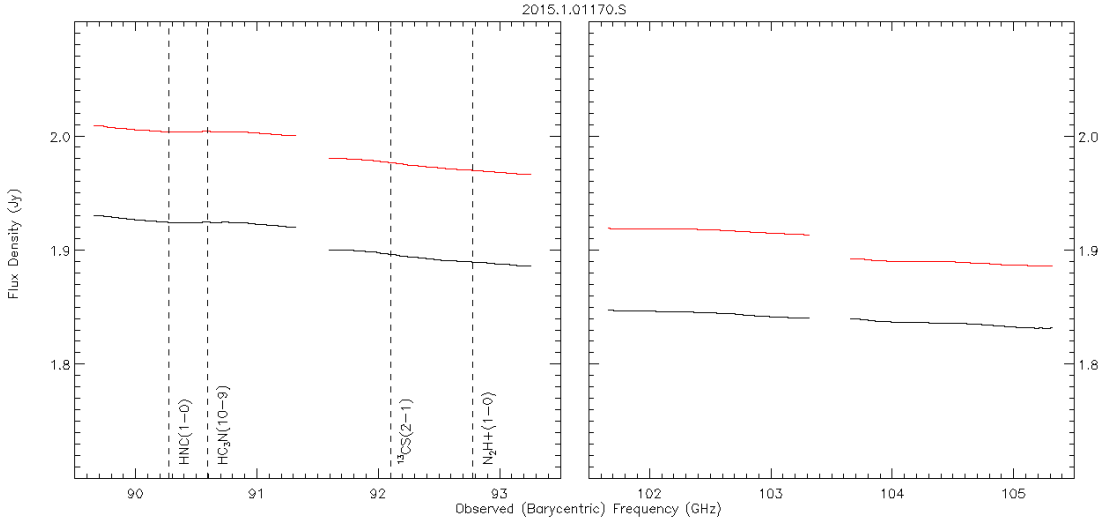

FIGURE A.2: 2015.1.01170.S continuum spectra

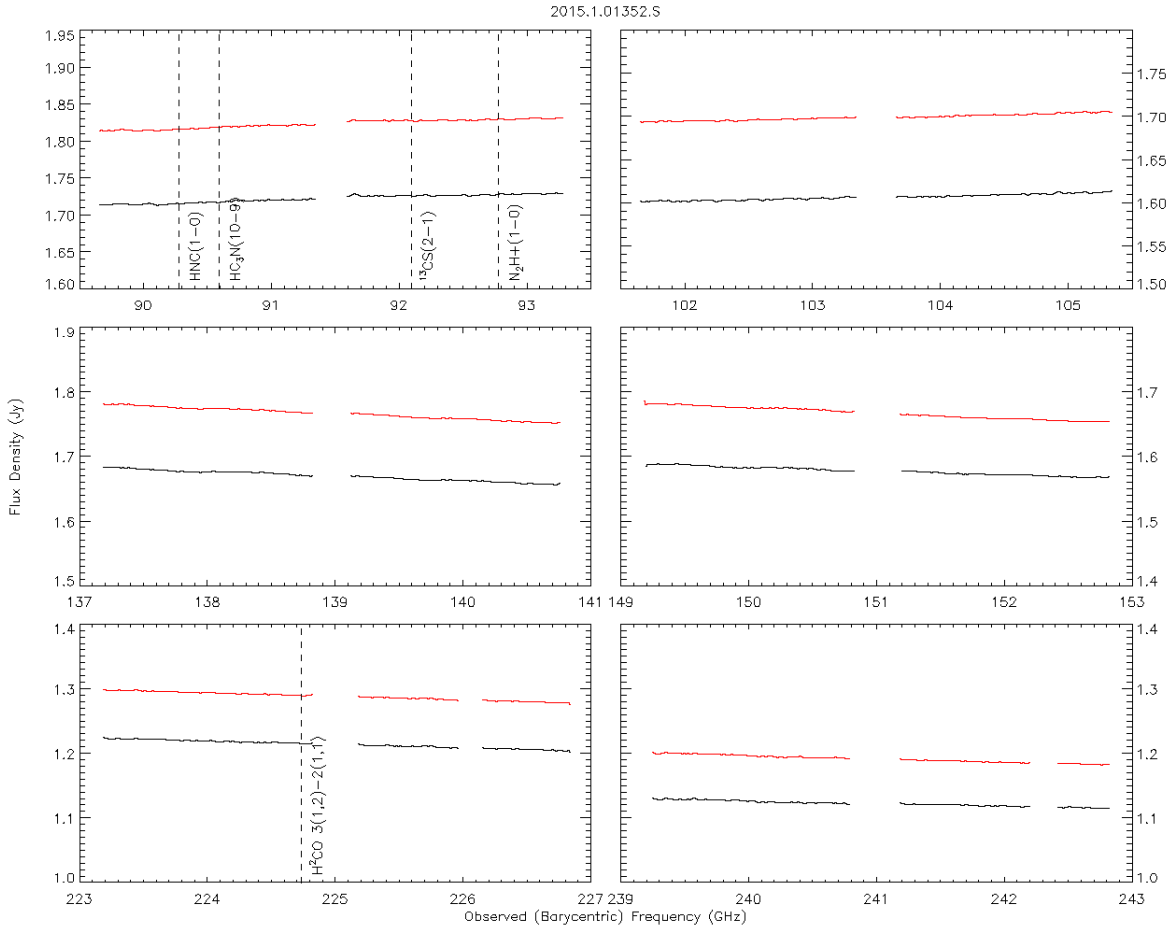

FIGURE A.3: 2015.1.01352.S continuum spectra. Observations from Oct 25 (top), Oct 31 (middle), and Oct 31 (bottom).

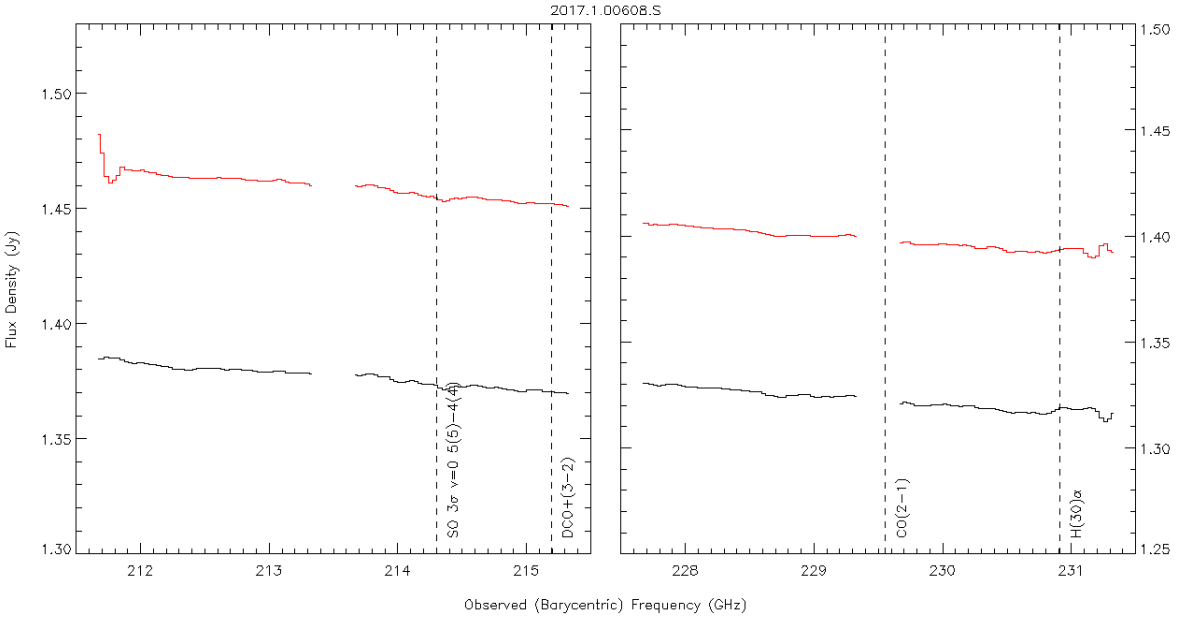

FIGURE A.4: 2017.1.00608.S continuum spectra.

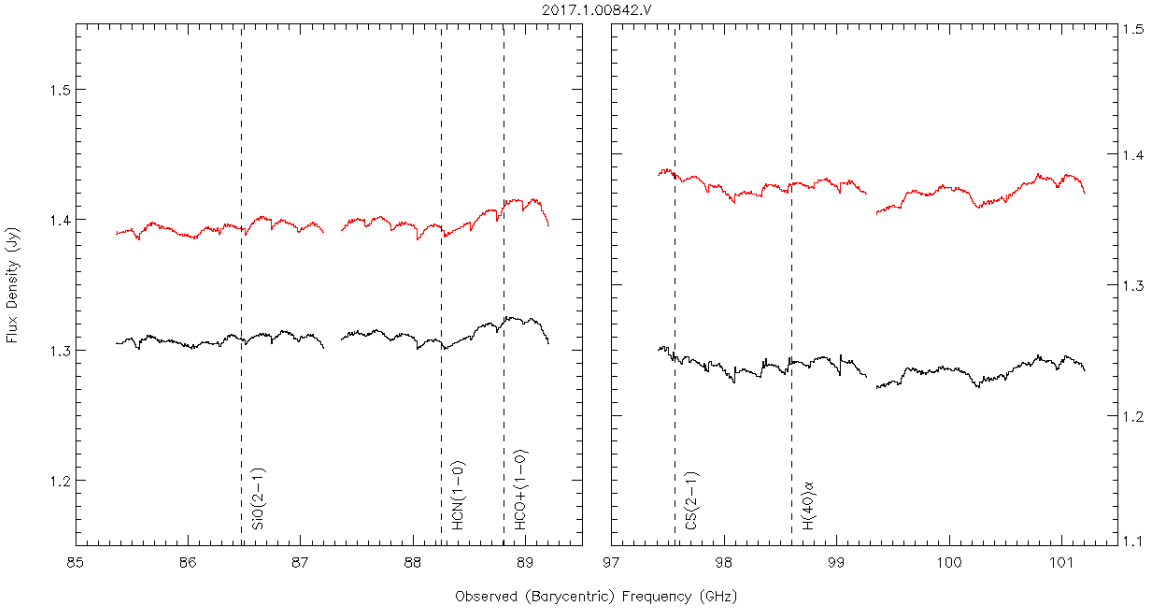

FIGURE A.5: 2017.1.00842.S continuum spectra

BIBLIOGRAPHY

Bieging, J. H., Blitz, L., Lada, C. J., & Stark, A. A. 1981, ApJ, 247, 443

Boizelle, B. D., Barth, A. J., Darling, J., et al. 2017, ApJ, 845, 170

Boizelle, B. D., Barth, A. J., Walsh, J. L., et al. 2019, ApJ, 881, 10

Braine, J., & Wiklind, T. 1993, A&A, 267, L47

Carilli, C. L., & Walter, F. 2013, ARA&A, 51, 105

Dwarakanath, K. S., van Gorkom, J. H., & Owen, F. N. 1994, ApJ, 432, 469

Eckart, A., Cameron, M., Genzel, R., et al. 1990, ApJ, 365, 522

Event Horizon Telescope Collaboration, Akiyama, K., Alberdi, A., et al. 2019, ApJ, 875, L6

France, K., Herczeg, G. J., McJunkin, M., & Penton, S. V. 2014, ApJ, 794, 160

Gebhardt, K., & Thomas, J. 2009, ApJ, 700, 1690

Güver, T., & Özel, F. 2009, MNRAS, 400, 2050

Neumayer, N., Cappellari, M., Reunanen, J., et al. 2007, ApJ, 671, 1329

North, E. V., Davis, T. A., Bureau, M., et al. 2019, MNRAS, 490, 319

Paine, S. 2019, The am atmospheric model, doi:10.5281/zenodo.3406483

Rose, T., Edge, A. C., Combes, F., et al. 2020, MNRAS, 496, 364

Sabra, B. M., Shields, J. C., Ho, L. C., Barth, A. J., & Filippenko, A. V. 2003, ApJ, 584, 164

Sandstrom, K. M., Leroy, A. K., Walter, F., et al. 2013, ApJ, 777, 5

Schulze, A., & Gebhardt, K. 2011, ApJ, 729, 21

Spilker, J. S., Marrone, D. P., Aguirre, J. E., et al. 2014, ApJ, 785, 149

Utomo, D., Blitz, L., Davis, T., et al. 2015, ApJ, 803, 16

Walsh, J. L., Barth, A. J., Ho, L. C., & Sarzi, M. 2013, ApJ, 770, 86